Annular Modes in a Multiple Migrating Zonal Jet Regime

Cegeon J. Chan, R. Alan Plumb, and Ivana Cerovecki

January 25, 2007

Program of Atmospheres, Oceans, and Climate, Department of

Earth, Atmospheric and Planetary Sciences,

Massachusetts Institute of Technology, Cambridge, Massachusetts

Corresponding address: Cegeon Chan, Department of Earth and Atmospheric Science,

MIT Building 54, Room 1719, 77 Massachusetts Avenue, Cambridge, MA, 02139

E-mail: cegeon@mit.edu

Abstract

We investigate the dynamics of zonal jets in a semi-hemisphere zonally-reentrant ocean model. The forcings imposed in the model are an idealized atmospheric wind stress and relaxation to a latitudinal temperature profile held constant in time. While there are striking similarities to the observed atmospheric annular modes, where the leading mode of variability is associated with the primary zonal jet's meridional undulation, secondary (weaker) jets emerge and systematically migrate equatorward.

The model output suggests the following mechanism for the equatorward migration. While the eddy momentum fluxes sustain the jets, the eddy heat fluxes have a poleward bias causing an anomalous residual circulation with poleward (equatorward) flow on the poleward (equatorward) flanks. By conservation of mass, there must be a rising residual flow at the jet. From the thermodynamics equation, the greatest cooling occurs at the jet core, thus creating a tendency to reduce the baroclinicity on the poleward flank, while enhancing it on the equatorward flank. Consequently, the baroclinic zone shifts, perpetuating the jet migration.

1 Introduction

In this paper, we describe some characteristics of zonal jets in a model of a zonally reentrant ocean, bounded by zonal walls at the equator and 50^oS, driven by a steady eastward wind stress which peaks in middle latitudes. The model simulation was run as a testbed for ideas on eddy transport, and its major, climatological, characteristics are described elsewhere (Cerovecki et al., 2007). Here we focus on the time variability of the zonal jets in the model. At any instant in time, the mean zonal flow comprises a dominant jet, together with two or three secondary jets, primarily on its poleward side. The main jet wobbles quasi-periodically, in a manner that appears similar to the "annular mode" behavior of atmospheric jets. At the same time, the secondary jets, poleward of the main jet, migrate systematically equatorward such that, once every period of the main jet's fluctuation, one secondary jet merges with the main jet, while another appears at the poleward flank of the secondary jets.

"Annular modes" are well documented in the atmosphere (*e.g.* Thompson and Wallace, 2000) as the dominant modes of non-seasonal atmospheric variability; they form deep dipole structures straddling the mean jet in each hemisphere, and describe north-south oscillations of the jets. Both analyses of observations and model studies show feedback between the mean flow and baroclinic eddies to be at the heart of the oscillations (*e.g.*, Robinson, 1994; Lorenz and Hartmann, 2001; Kushner and Polvani, 2004). Likewise, multiple jets have long been understood to occur in wide domains, and demonstrated in models ranging in complexity from barotropic and shallow water through to two-level quasi-geostrophic and multilevel primitive equation models (*e.g.*, Williams, 1978; Panetta, 1993; Cho and Polvani,

1996; Lee, 2005). Such structures have been observed in jets in the ocean (*e.g.*, Roden, 2000) and in the atmospheres of Jupiter and Saturn (*e.g.*, Pater and Lissauer, 2001). A recent discussion of the dynamics of the formation of multiple jet structures, and factors controlling their width, can be found in Dritschel et al. (2007). While most of these studies have not revealed any tendency for the jets to migrate, systematic equatorward migration of multiple jets, under some circumstances, has been described by Williams (2003) in a model of Jupiter's atmosphere.

There are two, related, points of interest in the present paper. First, the correspondence between the migration of the secondary jets and the oscillation of the main jet appears to be a manifestation of "annular mode" behavior in a multiple jet environment which, to our knowledge, has not been reported before. In fact, we shall show that most of the variance in the zonal flow is captured by two spatial structures, each of which projects onto both the main jet and the secondary jets and which, taken together, describe the simultaneous oscillation/migration pattern. Second, while the narrowness of the jets is maintained by eddy momentum fluxes (as has long been understood), their equatorward migration is a response to the eddy heat fluxes, which act to reduce the baroclinicity on the poleward flank of the jets and increase it on the equatorward flank. We speculate that this behavior is ultimately determined by the latitudinal gradient of the background static stability.

The structure of the paper is as follows. A cursory description of the model and its time-averaged features is presented in Section 2, an analysis of the spatial and temporal variability in section 3. Properties of the baroclinic eddies, their effect on the zonal mean

flow and, in particular, their relation to the migration of the secondary jets are discussed in section 4. Conclusions are summarized in Section 5.

2 Model Characteristics

The data in this study were generated by Cerovecki et al. (2007) from the MIT General Circulation Model (cf. Marshall et al. 1997a; Marshall et al. 1997b). Readers are referred to Cerovecki et al. (2007) for a complete description of the model setup and the equilibrated states. Here, we just provide a cursory description.

This is a zonally reentrant, semi-hemispheric model ranging from 50.67°S to 0.17°S and 0°E to 10° E on a $\frac{1}{6}^\circ \times \frac{1}{6}^\circ$ latitude/longitude grid with 15 vertical levels. The model does not include salinity; density is simply a linear function of temperature. The model-imposed forcings are shown in Fig. 1. The wind stress is eastward everywhere with weak winds near the equator. The heat forcing is applied to the upper surface layer, with a relaxation time of 30 days. Both forcings are constant in time and functions only of latitude. With the flow reaching statistically steady state by year 500, the model was integrated for a total of 1285 years, of which the last 313 years were examined for this study.

Time-averaged state

Despite the deformation radius increasing monotonically from about 10 km at 40°S to about 100 km at 15°S, the length scale of the forcings, shown in Fig. 1, are more than one to two orders of magnitude larger than the Rossby radius of deformation. With such a broad forcing,

it is not surprising that multiple jets emerge (Panetta 1993). Fig. 2 shows the time-mean zonal flow. A strong eastward jet (herein after the "main jet") is located at 17°S, while a weaker westward flow on its equatorward side. Poleward of the main jet is another eastward jet at about 26°. We shall see in what follows that this is the time-averaged remnant of several, time-dependent secondary jets.

Fig. 3 shows the time-averaged density and potential vorticity (PV) distributions. Poleward of 12°S, PV is homogenized along isopycnals in the near-adiabatic interior. This region of homogenized PV coincides with the region of baroclinic eddy activity (Cerovecki et al. 2007). PV gradients do appear in the non-adiabatic region near the surface, as is evident in Fig. 3, but the contribution in the surface "PV sheet" (Bretherton 1966) associated with the surface temperature gradient is not visible on the figure. To illustrate this point in the presence of multiple migrating jets, we show in Fig. 4(a) a snapshot of the zonally-averaged zonal flow, and (b) the quasi-geostrophic PV gradients integrated through the top 165 m (including the surface PV sheet) and (c) the quasi-geostrophic PV gradient at a typical interior level. As shown, the surface PV gradient dominates. Consistent with the arguments of Dritschel et al. (2007), each jet is associated with a sharp eddy-transport barrier. There are multiple PV "steps", i.e. the gradients are concentrated at each jet, and weak everywhere else. However, in our case the PV steps are manifested not in the interior, but rather in strong, localized gradients of surface temperature.

The static stability varies greatly in depth and in latitude, as indicated in Fig. 5. At any particular depth, the stability at all depths monotonically increases equatorward up to

approximately 20°S. As for the whole domain, several extrema are present. Perhaps, the most obvious is located between $-15°$ and $-10°$ above a depth of 750m, a region associated with mode water formation (Cerovecki and Marshall 2007).

3 Description of Variability

Fig. 6 shows the annual-mean zonal flow, year by year over a nine year period. While the main jet oscillates meridionally, two to three secondary jets migrate equatorward and each eventually merges with the main jet. Fig. 7 shows the vertically-integrated, zonally-averaged zonal flow anomalies as a function of latitude and time. The equatorward migration is clearly seen poleward of the primary jet, in particular, between 20°S and 35°S. From the emergence of the secondary jet around 30°S to the time it takes to reach the primary jet varies from 8 to 12 years and is a robust feature of this model.

Although less obvious, there is some evidence of zonal flow anomalies propagating poleward between $-10°$ and $-15°$. Compared to the equatorward migration at higher latitudes, the poleward propagation occurs less systematically and over a shorter range. Because of its close proximity to the main jet, entangling its influence with the zonal flow anomalies itself become difficult. Consequently, our discussions of propagating zonal flow anomalies will mainly focus on the region of systematic equatorward propagation between $-20°$ and $-30°$.

a. EOF Analysis

The spatial and temporal variability of the entire time series can be best quantified by the use of empirical orthogonal functions (EOFs). The data were weighted to account for the decrease in area around latitude circles toward the pole, but were not weighted to account for the varying layer depths. This will not be important as we are mostly interested in the horizontal variations of the zonal flow. Using the North et al. (1982) test, the first and second EOFs are-well separated.

Fig. 8 shows the horizontal structure of the leading two EOFs of the annually-averaged surface temperature. With the model forcings independent of longitude, it comes as no surprise that there is little longitudinal variability. Thus, for the remainder of the paper, we consider zonal-mean budgets and explicitly examine the variability of the zonally-averaged zonal flow.

As shown in Fig. 9, EOF1 displays an "equivalent barotropic" structure with maximum absolute anomalies at 19°S and 14°S. The vertical black line represents the time-averaged location of the primary jet's maximum value (17.2°S). By comparing the mode's spatial structure and the mean location of the jet, EOF1 describes meridional fluctuations of the main jet, or in other words, it captures the jet "wobbling" in the north-south direction. This mode constitutes the largest amount (39.5 percent) of the total variability. In EOF2, the maximum anomalies are almost coincident with the mean location of the jet. Therefore, this mode indicates the intensifying and weakening of the main jet. Given the structure of the EOFs in Figs. 8 and 9, therefore, the spatial variability near the primary jet appears to

be analogous to the atmospheric annular modes; the leading mode describes oscillations of the main jet, while the second mode captures its enhancement (*e.g.* Lorenz and Hartmann 2001) just as it does in the atmospheric eddy-driven jet.

Unlike the atmospheric case, there is an obvious non-dipole structure in both modes; poleward of 20°S, three to four more additional extrema are present. These features capture the migrating secondary jets, with EOF2 comparable in magnitude with, and in quadrature with, EOF1 in this region. Thus EOF2 must account for more variance than is typical in the atmospheric case. Higher order components are weaker with EOF3 capturing eleven percent and successive EOFs less than four percent; therefore, as Fig. 10 shows, the evolution of the zonal flow is well captured by the first two EOFs (*cf.* Fig.6).

b. Description of EOF phases

The principal component captures the temporal variations associated with the spatial pattern of the EOFs. For instance, when the primary jet is displaced poleward (equatorward), the principal component associated with EOF1, PC1, will be positive (negative). Similarly, when the zonal flow at the primary jet is anomalously positive (negative), the principal component associated with EOF2, PC2, will be positive (negative).

Now that we have established how well the variability in the zonal average of $u(y, z, t)$ is represented by the two EOFs, we define the following four phases (shown in Table 1) to capture both the temporal and spatial variability. For instance, we define Phase A as PC1$<$0 and PC2$<$0, Phase B as PC1$<$0, PC2$>$0, etc. A graphical representation of the four phases

is shown in Fig. 11, as well as an example of a twenty-one year time series in the PC space. Throughout the 313-year time series, there is a sense of generally clockwise rotation, such that the following sequence occurs: Phase A $\rightarrow$ Phase B $\rightarrow$ Phase C $\rightarrow$ Phase D and then repeats back to Phase A. Since the secondary jets migrate, the principal components of both modes need to change sign to allow the secondary jets to advance equatorward and hence, this sequence is ultimately dictated by the behavior of the secondary jets.

Now that we have defined these four phases of the oscillation, we can thus describe the evolution of the structure of the zonal mean state as well as eddy fluxes by compositing all years associated with each phase. When analyzing migrating jets, a time-average would "smooth" out its spatial structure. However, by defining these four phases, we will now be able to capture and examine the migrating jets. An example, which will be discussed in greater detail later, is shown in Fig. 17. The sequence shows that the primary jet wobbles, while the secondary jets migrate equatorward, precisely the behavior shown in Fig. 6. We can think of this sequence as a typical eight year cycle with each phase representing roughly two years.

Table 2 shows how closely the sequence was followed. Each change in phase is followed by the correct phase at least sixty-four percent of the time, e.g. the conditions prior to the onset of Phase A were correctly described to be in Phase D sixty-four percent of the time and incorrectly by Phase B or C thirty-six percent of the time. Similarly, Phase A described the PC space prior to Phase B eighty-five percent of the time. This shows that these pre-conditions are not symmetric, e.g. there is a stronger relation between Phase A and Phase

B than there is between Phase D and Phase A.

Given the results in Table 2 and Fig. 17, there is a correlation between the strengthening of the main jet and the arrival of the migrating jets. When the secondary jet is closest (Phases B and C), there is also an intensification of the primary jet (see Table 1). The implication is that as the migrating jet approaches, the main jet intensifies then displaces poleward (Phase C), the side of the approaching secondary jet. Conversely, in Phases A and D, where the strength of the main jet decreases, the closest secondary jet is further away.

One last statistical result worth mentioning, brings attention to the duration of each phase. For our 313-year model study, Phase A constituted 95 years in total, nearly twenty percent more than any other phase. Concurrent with anomalous weak eddy activity, the low zonal index (i.e. when PC1 is negative) lasting for longer durations appears consistent with the study done by Feldstein and Lee (1996), who examined the zonal index of the atmospheric jet in an aquaplanet.

4 The role of eddies in the flow evolution

The zonal flow anomalies shown in Fig. 7 are observed to persist on time scales that are larger than the frictional timescale associated with the bottom drag. Eddy-mean flow interaction is the only process capable of maintaining these anomalies.

a. Vertically integrated momentum budget

The zonal momentum equation for quasi-geostrophic motion can be written as:

$$\frac{\partial[u]}{\partial t} - f[v] = -\frac{\partial[u'v']\cos^2\phi}{a\cos^2\phi\partial\phi} + \frac{\partial[\tau]}{\partial z} \tag{1}$$

where square brackets represent zonal averages, primes denote deviations therefrom, τ represents the applied forcing and the bottom friction. Integrating the entire column, we obtain:

$$\frac{\partial < [u] >}{\partial t} = -\left\langle \frac{\partial[u'v']\cos^2\phi}{a^2\cos^2\phi\partial\phi} \right\rangle + [\tau_{surf}] - [\tau_{bot}] \tag{2}$$

where vertically-integrated values are represented by angle brackets, the Coriolis force vanishes owing to mass conservation, τ_{surf} is the applied wind forcing shown in Fig. 1a; the bottom stress, τ_{bot}, is calculated in the model as:

$$\tau_{bot} = 2A_z\frac{u_{bot}}{\delta_{bot}} + C_D u_{bot}\sqrt{\frac{1}{2}(u_{bot}^2 + v_{bot}^2)} \tag{3}$$

where A_z is the vertical viscosity, u_{bot} and v_{bot} is the zonal and meridional velocity, respectively, at the bottom of the ocean, δ_{bot} is the thickness of the bottom layer, C_D is the bottom drag coefficient. (For specific values, see Cerovecki et al. 2007.)

The time-averaged momentum budget is discussed in Cerovecki et al. (2007). The three terms on the right-hand side of (2) must balance. The wind stress is balanced, on the broad scale, by bottom drag. However, there are spatial variations in the latter on the jet scale that do not correspond to features in the wind stress; rather, these variations balance the convergence of eddy momentum fluxes (e.g. Held 1975; Ioannou and Lindzen 1986.)

Since we are interested in the equatorward migration of the zonal flow anomalies, we will

here examine departures from the time mean of (2). Since the wind forcing was held constant in time, there is only a three-way balance between the vertically-integrated flow tendency, anomalous convergence of the eddy momentum flux, and the anomalous bottom drag. After taking departures from the time-averaged state, Fig. 13 shows composites of each phase as described in the previous section. There is a quasi-steady balance between the bottom drag and the divergence of the Reynolds' stress, the flow tendency being weak and virtually negligible compared to these two terms. The zonal flow anomalies are therefore sustained by the anomalous convergence of eddy momentum fluxes. Note that there is no obvious latitudinal bias in the momentum flux convergence. Thus, another approach is needed to explain why the jets are migrating equatorward.

b. Eddy-Mean Flow Interaction

In order to understand fully the effect of the eddies on the mean flow, we use the transformed Eulerian mean (TEM) appraoch. This allows us to consider simultaneously the effects of the eddy momentum and heat fluxes (we shall in fact see that the heat budget plays a large role in the jet migration). The quasi-geostrophic TEM equations are (Andrews and McIntyre 1976):

$$\frac{\partial [u]}{\partial t} - f[\widetilde{v}^*] = \nabla \cdot \mathbf{F} + \frac{\partial \tau}{\partial z} \tag{4}$$

$$\frac{\partial [T]}{\partial t} + [\widetilde{w}^*]\frac{\partial T}{\partial z} = Q \tag{5}$$

where Q represents diabatic effects,

$$\mathbf{F} = (F_y, F_z) = \Big(- [u'v'], f\frac{[v'T']}{[T_z]} \Big) \tag{6}$$

is the Eliassen-Palm (EP) flux vector (*e.g.* Edmon et al. 1980), and

$$\widetilde{v}^* = [v] - \frac{\partial}{\partial z}\frac{[v'T']}{T_z} \tag{7}$$

$$\widetilde{w}^* = [w] + \frac{\partial}{\partial y}\frac{[v'T']}{T_z} \tag{8}$$

is the residual circulation.

Once again, since we are interested in the departures from the time-mean, (4) can be simplified. Away from the surface, we may neglect Q because there are no significant diabatic effects in the interior. Since the applied wind stress is constant in time, its anomalous value is always zero. Further, the bottom friction can be neglected when we focus our attention between the surface and the top 1600m (where the activity is strongest). Thus, (4) and (5) can be rewritten as:

$$\frac{\partial [u]}{\partial t} - f\,[\widetilde{v}^*] = \nabla \cdot \mathbf{F} \tag{9}$$

$$\frac{\partial [T]}{\partial t} + [\widetilde{w}^*]\,\frac{\partial [T]}{\partial z} = 0 \tag{10}$$

where all the above terms represents deviations from the time-average.

Near the surface, we invoke Bretherton's PV sheets (Bretherton 1966), exploiting the equivalence between an inhomogeneous boundary temperature distribution and a delta function PV anomaly just inside an isothermal boundary. Then both F_z and $[\tilde{w}^*]$ vanish at the boundary, and the divergence of EP fluxes are concentrated in the surface PV sheet.

Accordingly, we first vertically integrate each of the terms in (9) through the top 1600 m for each phase of the evolution; the results of doing so are shown in Fig. 14. There are three important features to note. First, the flow tendency is essentially a residual; the local momentum budget for each phase is a quasi-steady balance between the anomalous divergence of the EP fluxes and the TEM Coriolis term. Second, the baroclinic component $\partial F_z/\partial z$ dominates over the barotropic component $\partial F_y/\partial y$ in the divergence of the EP flux. Third, the anomalous EP flux divergence is out of phase with the secondary jets; the strongest anomalous convergence lies on the poleward flank, while the strongest anomalous divergence occurs on the equatorward flank. The reason behind the spatial structure of $\nabla \cdot \mathbf{F}$ will be discussed further in the next section.

The anomalous $\nabla \cdot \mathbf{F}$ thus creates an anomalous residual circulation as shown in Fig. 15 (and schematically illustrated in Fig. 20b). On the poleward (equatorward) flanks of an anomalous eastward jet, the EP flux is convergent (divergent), producing a poleward (equatorward) residual flow. By conservation of mass, near the jet cores, the anomalous residual flow must rise and, in between the jets, must sink.

From (10), the rising residual circulation implies the temperature tendency is a local

minimum near the secondary jets (see Fig. 16). Therefore, the time tendency for the meridional temperature gradient is positive on the equatorward flank and negative on the poleward flank, thus encouraging equatorward migration of the baroclinic zone. From the thermal wind relation, vertical shear will increase (decrease) on the equatorward (poleward) side, furthering the equatorward jet migration. Thus, this pattern of strong/weak baroclinic jets moving equatorward is ultimately dictated by the pattern of the EP flux divergence.

c. EP fluxes

We have seen, therefore, that the equatorward migration of the secondary jets is a consequence of the structure of $\nabla \cdot \mathbf{F}$, in particular, the fact that the anomalous near-surface EP flux convergence is located on the poleward flank of each eastward jet, rather than at the jet center, as one might naïvely expect. This finding, in turn, begs the question, why are the fluxes organized in this way?

Before examining the anomalous EP fluxes, we show in Fig. 17 the total EP fluxes for each of the four phases described in section 3. In all cases, equatorward of 12°S, where the isopycnals are relatively flat, little to no eddy activity is observed. However, eddies are ubiquitous poleward of 12°S. In all phases, the flux is upward (i.e. eddy heat flux is poleward), consistent with baroclinic instability being the source of the eddies. Comparing the different phases, both the eddy heat flux and eddy momentum flux are more dominant in the high index phases C and D than in the low zonal index phases A and B.

Since our interest is in the time-varying jets, we now focus on the anomalous EP flux

vectors (i.e. departures from the time-mean) shown in Fig. 18. In general, where there are positive zonal flow anomalies, the baroclinic component of the flux is enhanced (more upward). However, upon a closer examination, the maximum of F_z is not coincident with the jet and is not symmetric: there is a poleward bias. From (6), the asymmetry must exist in the anomalous zonally-averaged eddy heat flux or in the static stability. (We presume that variation in Coriolis parameter across these narrow jets is too small to be of significance.) In fact, as Fig. 19 demonstrates, the composites of each phase indeed show that there is a robust poleward bias in the anomalous eddy heat flux.

Why are the largest poleward eddy heat fluxes located poleward of the eastward zonal flow anomaly? We speculate that the implied asymmetry in baroclinic eddy activity is consistent with a bias in the Eady growth rate (Eady 1949), defined to be:

$$\sigma \propto \frac{fU_z}{N}. \tag{11}$$

We use σ as a local measure of instability, and speculate that the upward EP fluxes of baroclinic eddies will maximize where σ is greatest. The Coriolis parameter varies only by a factor of between five to eight percent in the region of interest over the typical width (about 2 degrees) of the jets. The vertical shear is essentially symmetric about the secondary jets. However, the buoyancy frequency, N, varies systematically with latitude in the region poleward of the main jet (see Fig. 5). In the migrating jet regime, N varies from thirty percent to over fifty-five percent over the length scale of the jets, with smaller values on the poleward side. Thus, the absolute magnitude of the Eady growth rate is larger on the

secondary jets' poleward flank, consistent with the stronger poleward eddy heat fluxes there. Therefore, with N increasing monotonically equatorward in the migrating jet region, we speculate that, in the absence of any other asymmetries, the latitudinal variation in the background static stability may produce the asymmetry in the eddy heat fluxes.

d. Summary of the eddy-mean flow interaction

Drawing all these results together, the nature of the interaction between the eddies and the evolving jets is summarized schematically in Fig. 20. In the absence of any latitudinal asymmetries in the background state, one might expect the situation depicted in frame (a), the EP fluxes being symmetric about the jet, with divergence beneath the jet and convergence at and near the surface. Given our finding that the time derivative in (9) is negligible, the consequence is a pumping of the residual flow poleward at and near the surface, and equatorward at the bottom, generating a circulation cell as shown. The residual upwelling and downwelling therefore produce cooling on the equatorward flank, and warming on the poleward flank, of the jet, thereby reducing the baroclinicity at the jet core, and enhancing it at the flanks. This symmetric pattern would induce no tendency of the baroclinic zone, and the consequent jet, to migrate.

Consider now frame (b), in which we assume that the baroclinic eddy activity is displaced poleward of the jet as a consequence of basic state static stability increasing equatorward in the background state. The residual circulation cell is, accordingly, displaced poleward with respect to the jet, thus producing tendencies of reducing baroclinicity on the poleward

flank, and enhancing it on the equatorward flank, leading to equatorward migration of the baroclinic zone and therefore of the jet itself.

5 Conclusions

As was shown in Fig. 6, multiple zonal jets emerge when extremely broad buoyancy and wind forcing are applied to the surface of the model ocean. Although both forcings are constant in time, there is significant variability in the zonally-averaged zonal flow (see Fig. 7). Between 15°S and 20°S, the main eastward jet oscillates meridionally, while between 20°S and 35°S, secondary (weaker) jets systematically migrate equatorward. An EOF analysis describes the leading mode as an equivalent barotropic structure with the largest anomalies 3° north and south of the primary jet's time-averaged position, thus describing north-south fluctuations of the main jet, in a manner qualitatively similar to atmospheric behavior (*e.g.* Thompson and Wallace 1998). However, unlike the atmospheric case, the two leading EOFs are in quadrature in the region of the secondary jets where, together, they capture the jets' migration.

The secondary jets are maintained against bottom friction by convergence of the eddy momentum fluxes. However, it is the eddy heat fluxes (or equivalently, the vertical component of the EP fluxes) that control their equatorward migration. Although the anomalous convergence of the eddy momentum flux is nearly symmetric along the jet axis, convergence of the baroclinic (vertical) component of the EP flux is not. The vertical EP flux dominates locally and is stronger on the poleward flank of the jets (see Fig. 14), leading to the jets'

equatorward migration. We speculate that the asymmetry in the vertical EP flux is consistent with larger Eady growth rates associated with smaller values of static stability on the poleward side of the jets.

Recall from Section 3 that equatorward of the main jet, there is some evidence (cf. Fig 7) of poleward migration of zonal flow anomalies, although this migration is not as systematic as the equatorward migration further poleward. As Fig. 5 makes clear, the latitudinal structure of the static stability changes character equatorward of the main jet. Below the depth of about 1000m, its gradient changes sign, at about 14°S (though the gradient is weak equatorward thereof); about 1000m, the structure is more complex. Therefore it is difficult to relate the behavior of the flow anomalies to the static stability structure in this region.

We might therefore expect equatorward (or poleward) migration of baroclinic jets whenever the static stability or, more generally, N/f, increases (or decreases) equatorward throughout the vertical column. In fact, the multiple jets described by Williams (2003), either migrated equatorward or remained steady, depending on the background state. In the non-migrating cases, at altitudes of strongest baroclinic activity, there were little to no latitudinal variations of the vertical temperature gradient (Williams' Fig. 6a). However, in the migrating jet cases, the inferred static stability increased monotonically equatorward (Williams' Fig. 6b), consistent with the mechanism described above. Further, the patterns of EP flux divergence, in relation to the jets, showed similar characteristics to those described here.

Although observational records depict poleward migrating behavior in the observed atmosphere (Feldstein 1998), the mechanism discussed in this study may still be relevant.

Other theories have been proposed in describing this behavior (*e.g.* James et al. 1994; Lee et al. 2007). Here, we note that above the boundary layer, at all heights, the static stability increases poleward (Peixoto and Oort 1992). Assuming no other asymmetries, larger Eady growth rates would be larger on the equatorward side and a similar argument discussed above would hold. While this may be a coincidence, the potential for waves to develop more strongly in a region of lower static stability leading to the poleward propagation of zonal flow anomalies warrants further study.

While there's a distinct migration in the atmosphere, whether this behavior arises in the observed ocean is uncertain. Perhaps limited by the length of observational records with sufficient spatial resolution encompassing a large enough domain, we are unaware of any documented observations reporting migrating jets. However, in the Antarctic circumpolar current (ACC), there are three important ingredients that would make this region a possibility. First, multiple jets have been reported (Nowlin and Klink 1986), and, secondly, as a zonally reentrant channel, this is similar to our idealized model. Finally, away from the mixed layer, the static stability monotonically increases equatorward from 0 s^{-1} to about $3x10^{-3}$ s^{-1} (Levitus et al. 1994). Therefore, migrating behavior in the ACC cannot be ruled out and merits further research.

6 Acknowledgements

We wish to thank three anonymous reviewers for their beneficial comments on this manuscript. This research was supported by the National Science Foundation under grants

OCE-0426307 and ATM-0314094.

References

Andrews, D. G. and M. E. McIntyre, 1976: Planetary waves in horizontal and vertical shear: The generalized eliassen-palm relation and the mean zonal acceleration. *J. Atmos. Sci.*, **33**, 2031–2048.

Bretherton, F. P., 1966: Critical layer instability in baroclinic flows. *Quart. J. Roy. Meteor. Sob.*, **92**, 325–334.

Cerovecki, I. and J. C. Marshall, 2007: Eddy modulation of air-sea interaction and convection. *submitted to J. Phys. Oceanogr.*

Cerovecki, I., R. A. Plumb, and W. Heres, 2007: Eddy transport and mixing in a wind and buoyancy driven jet on the sphere. *submitted to J. Phys. Oceanogr.*

Cho, J. Y.-K. and L. M. Polvani, 1996: The emergence of jets and vorticies in freely evolving, shallow-water turbulence on a sphere. *Phys. Fluids*, **8**, 246–262.

Dritschel, D. G., P. H. Haynes, and M. E. McIntyre, 2007: Multiple jets as pv staircases: the phillips effect and the resilience of eddy-transport barriers. *submitted to J. Atmos. Sci.*

Eady, E. T., 1949: Long waves and cyclone waves. *Tellus*, **1**, 35–52.

Edmon, Jr., H. J., B. J. Hoskins, and M. E. McIntyre, 1980: Eliassen-Palm cross-sections for the troposphere. *J. Atmos. Sci.*, **37**, 2600–2615.

Feldstein, S., 1998: An observational study of the intraseasonal poleward propagation of zonal mean flow anomalies. *J. Atmos. Sci.*, **55**, 2516–2529.

Feldstein, S. and S. Lee, 1996: Mechanisms of zonal index variability in an aquaplanet GCM. *J. Atmos. Sci.*, **53**, 3541–3556.

Held, I. M., 1975: Momentum transport by quasi-geostrophic eddies. *J. Atmos. Sci.*, **32**, 1494.1497.

Ioannou, P. and R. S. Lindzen, 1986: Baroclinic instability in the presence of barotropic jets. *J. Atmos. Sci.*, **43**, 2999–3014.

James, P., K. Fraedrich, and I. N. James, 1994: Wave-zonal-flow interaction and ultra-low-frequency variability in a simplified global general circulation model. *Quart. J. Roy. Meteor. Sob.*, **120**, 1045–1067.

Kushner, P. J. and L. M. Polvani, 2004: Stratosphere-troposphere coupling in a relatively simple AGCM: The role of eddies. *J. Climate*, **17**, 629–639.

Lee, S., 2005: Baroclinic multiple zonal jets on the sphere. *J. Atmos. Sci.*, **62**, 2484–2498.

Lee, S., S. Son, and K. Grise, 2007: Mechanism of poleward propagation of zonal mean flow anomalies. *submitted to J. Atmos. Sci.*

Levitus, S., R. Burgett, and T. Boyer, 1994: *World Ocean Atlas 1994. Vol 3: Salinity; Vol. 4: Temperature. NOAA Atlas NESDIS 3 and 4.* U.S. Dept. of Commerce.

Lorenz, D. J. and D. L. Hartmann, 2001: Eddy-zonal flow feedback in the Southern Hemisphere. *J. Atmos. Sci.*, **58**, 3312–3327.

Marshall, J., A. Adcroft, C. Hill, L. Perelman, and C. Heisey, 1997: A finite-volume, incompressible Navier Stokes model for studies of the ocean on parallel computers. *J. Geophys. Res.*, **102**, 5753–5766.

Marshall, J., C. Hill, L. Perelman, and A. Adcroft, 1997: Hydrostatic, quasi-hydrostatic, and nonhydrostatic ocean modeling. *J. Geophys. Res.*, **102**, 5733–5752.

North, G. R., T. L. Bell, R. F. Cahalan, and F. J. Moeng, 1982: Sampling errors in the estimation of empirical orthogonal functions. *Mon. Wed. Rev.*, **110**, 699–706.

Nowlin, W. D. and J. M. Klink, 1986: The physics of the antarctic circumpolar current. *Rev. Geophys.*, **24**, 469–491.

Panetta, R. L., 1993: Zonal jets in wide baroclinically unstable regions: persistence and scale selection. *J. Atmos. Sci.*, **50**, 2073–2106.

Peixoto, J. P. and A. H. Oort, 1992: *Physics of Climate*. Springer, 564 pp.

Robinson, W. A., 1994: Eddy feedbacks on the zonal index and eddy-zonal flow interactions induced by zonal flow transience. *J. Atmos. Sci.*, **51**, 2553–2562.

Roden, G., 2000: Flow and water property structures beween the Bering Sea and Fiji in the summer of 1993. *J. Geophys. Res.*, **105**, 28,595–28612.

Thompson, D. W. J. and J. M. Wallace, 1998: The Arctic Oscillation signature in the wintertime geopotential height fields. *Geophys. Res. Lett.*, **25**, 1297–1300.

Thompson, D. W. J. and J. M. Wallace, 2000: Annular modes in the extratropical circulation. Part I: Month-to-month variability. *J. Climate*, **13**, 1000–1016.

Williams, G., 1978: Planetary circulations: 1. Barotropic representation of Jovian and terrestrial turbulence. *J. Atmos. Sci.*, **35**, 1399–1426.

Williams, G. P., 2003: Jovian dynamics. Part III: Multiple, migrating, and equatorial jets. *J. Atmos. Sci.*, **60**, 1270–1296.

List of Figures

Positive contours start at 20 and increase in increments of 200. Negative contours (dashed lines) start at -200 and are also in increments of 200. Thick black line represents the time-averaged position of the main jet.

Figure 8 The leading two EOFs of the annually-averaged temperature at the surface layer. The percent variance is shown in the bottom left corner.

Figure 9 The leading two EOFs of the annually-averaged zonal-mean zonal flow. Solid (dashed) lines represent positive (negative) values. Note the nonuniform contour interval. Vertical black line indicates position of the time-averaged jet. The percent variance is shown in the bottom right corner.

Figure 10 Time series of the reconstructed zonal flow using the leading two EOF modes and the time-averaged zonal flow.

Figure 11 The time series of the leading two principal components in PC space. The EOF phases are described in Table 1 and labelled in each quadrant. Each point is a one year average.

Figure 12 (a) Time-averaged quantities of the vertically-integrated zonally-averaged zonal momentum budget. Adapted from Cerovecki et al. (2007) (b) Time average of the vertically-integrated eddy momentum flux $< [u'v'] >$.

Figure 13 Anomalous quantities of the vertically-integrated zonally-averaged zonal momentum budget for each EOF phase composite labelled at the bottom left corner of each plot. Blue (solid) line is the flow tendency; green (long dashed) line is the eddy momentum flux convergence; red (vertically dashed) line is the friction. Black (vertical) dashed lines corre-

spond to the maximum positive zonal flow anomalies.

Figure 14 Anomalous quantities of the vertically-integrated TEM equation for each phase. The vertical integral was taken from the surface to a depth of 1600m. Blue (solid) line is the divergence of the vertical component of the EP flux; green (long dashed) line is the divergence of the horizontal component of the EP flux; red (dotted) line is the flow tendency; and the cyan (dot-dashed) line is the Coriolis force. Black (vertical) dashed lines correspond to the maximum positive zonal flow anomalies.

Figure 15 Anomalous residual circulation (vector) plotted over anomalous zonal flow (color) for each phase. The vectors are scaled the same for each plot, with the largest vector corresponding to 1.33 cm sec^{-1}.

Figure 16 Anomalous quantities of the transformed Eulerian mean thermodynamic equation ($^oC\ s^{-1}$) at z=-593m. Blue (solid) line is the temperature tendency; green (long dashed) line is the residual vertical advection of the vertical temperature gradient; red (dot dashed) line is the residual meridional advection of the meridional temperature gradient. Black (vertical) dashed lines correspond to the maximum positive zonal flow anomalies.

Figure 17 The total EP flux vectors for each EOF phase composite (labelled on bottom left corner) along with the zonally-averaged zonal flow. The vectors are scaled the same for each plot.

Figure 18 Anomalous EP flux vectors for each EOF phase composite are plotted over the zonally-averaged zonal flow anomalies. Each phase is labelled at the bottom left corner of plot. The vectors are scaled twice as large as Fig. 17 and are the same for each plot.

Figure 19 Anomalous eddy heat flux (line) is plotted over zonal flow anomalies (in color). Each phase is labelled at the bottom left corner of plot.

Figure 20 Schematic depiction of the interaction between baroclinic eddies and a localized jet. In frame (a), the baroclinic eddy activity is assumed to be symmetric about the jet; in (b), it is stronger on the poleward flanks of the jet, presumed to be a consequence of a general poleward decrease of static stability. 'CONV' and 'DIV' denote convergence and divergence, respectively, of the baroclinic EP fluxes; 'COOL' and 'WARM' indicate the local temperature tendencies attributable to the induced residual circulation, thus reducing ($\mathcal{R}$) and enhancing ($\mathcal{E}$) the local zonal mean baroclinicity. (Note that the southern hemisphere is depicted; the equator is to the right.) See text for discussion.

List of Tables

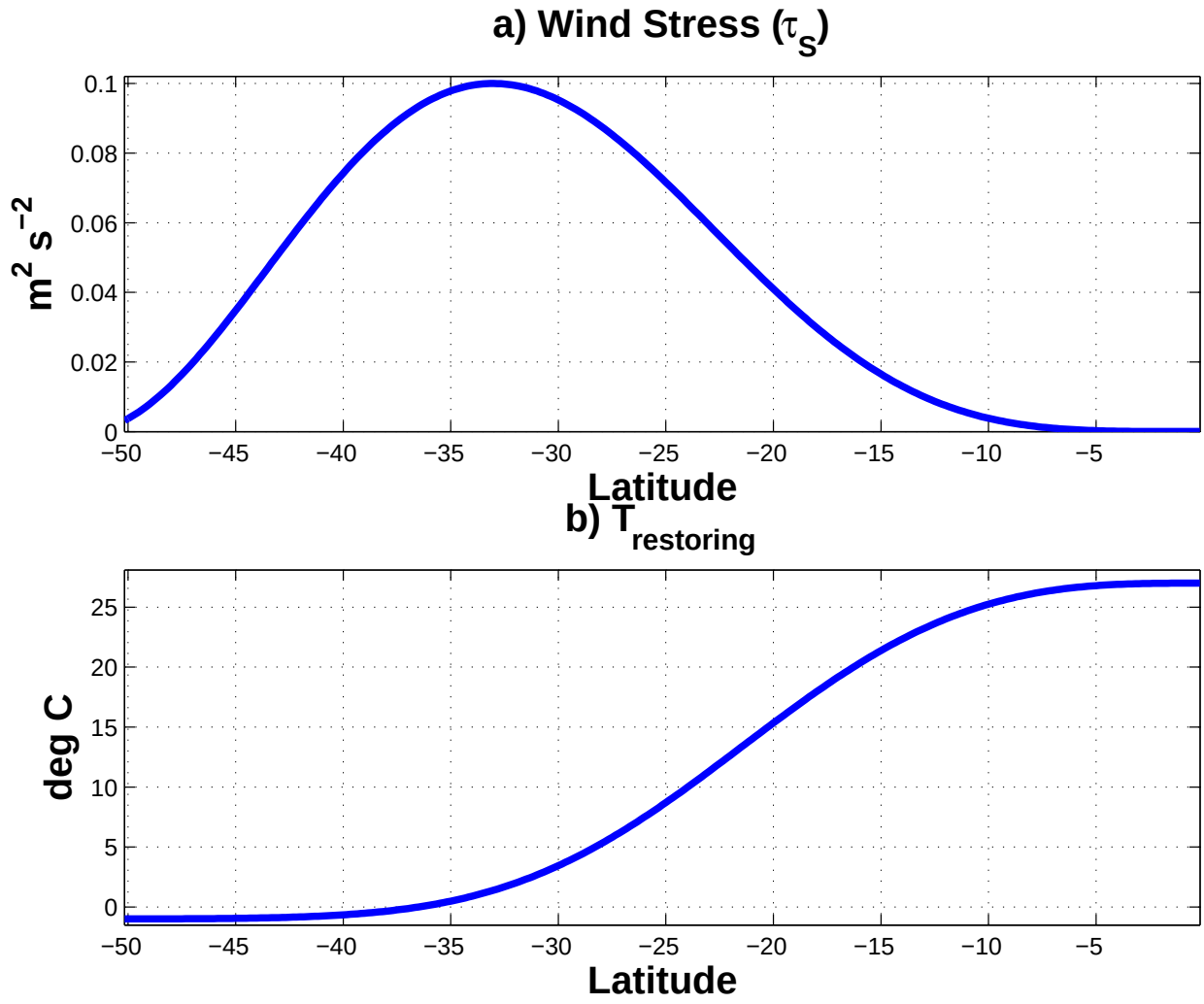

Figure 1: The prescribed model forcings are an (a) atmospheric wind stress and (b) heat forcing with a relaxation time of order one month. Both are constant in time, only a function of latitude, and applied to the top surface layer (22m). Adapted from Cerovecki et al. (2007).

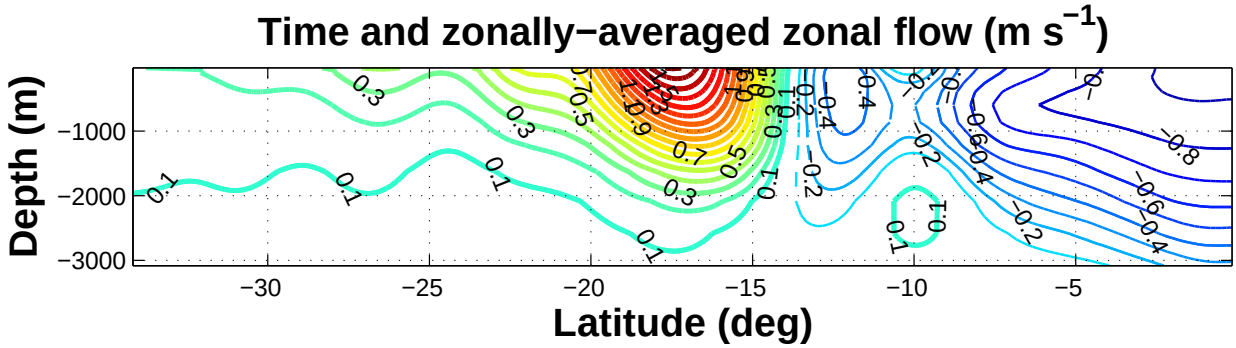

Figure 2: Time and zonally-averaged zonal flow. Contour interval is 0.1 m s^{-1}. Zero contour is omitted.

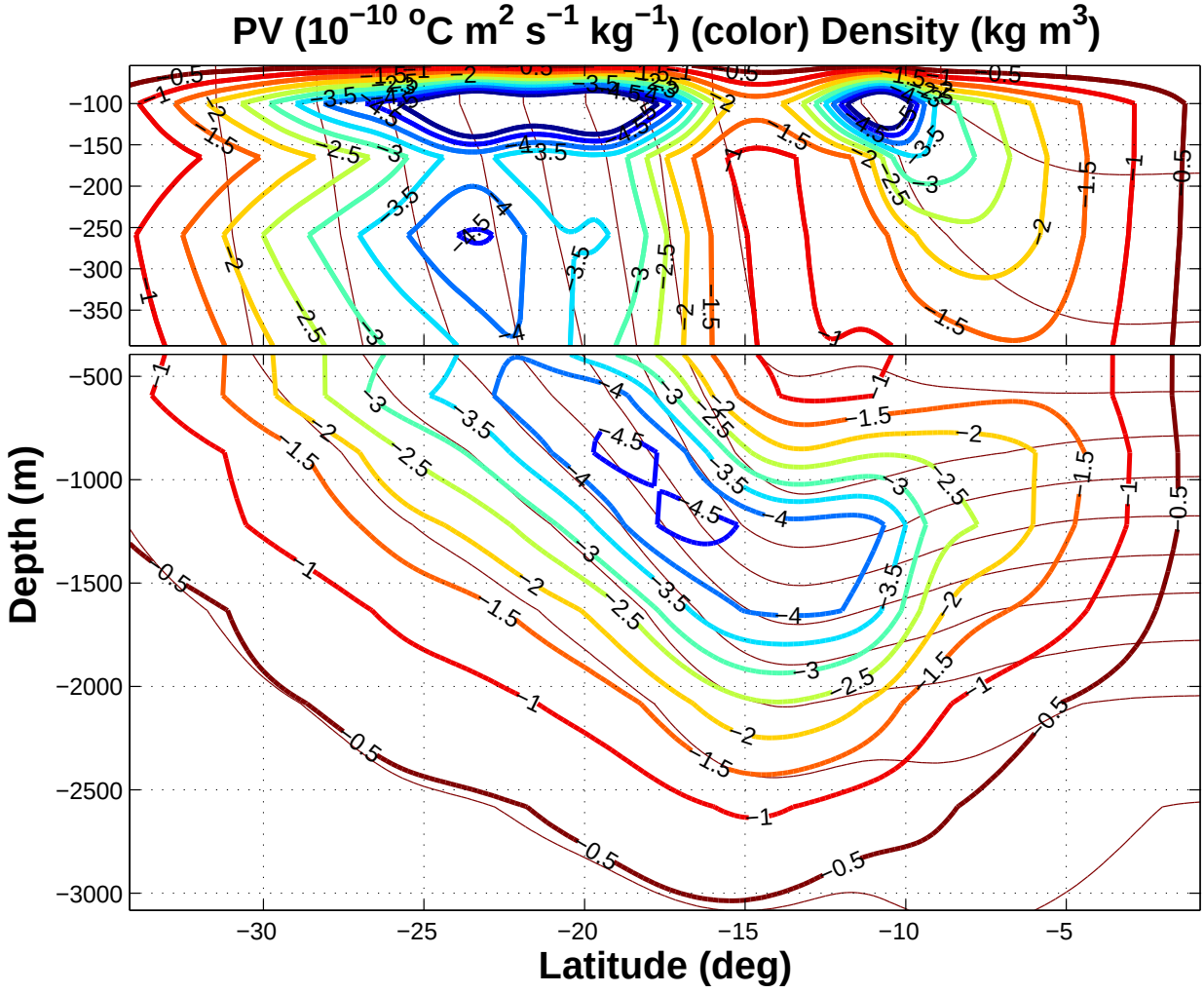

Figure 3: Time-averaged quantities of Ertel's potential vorticity (thick line) and isopycnals (thin line) with a contour interval of 0.5 x 10^{-10} °C m^2 s^{-1} kg^{-1} and 0.5 kg m^{-3}, respectively. Note the top 400m has been enlarged.

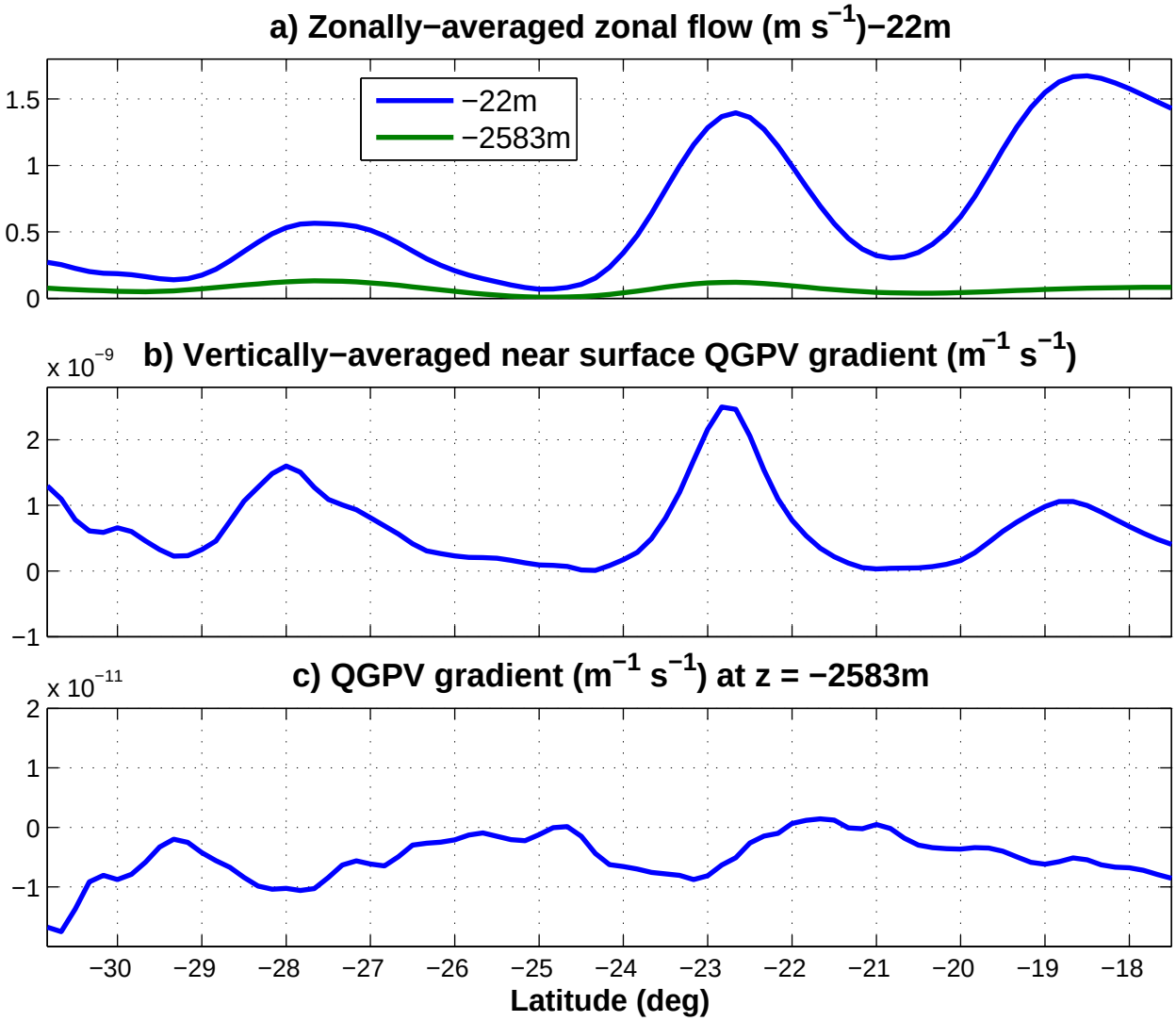

Figure 4: Snapshot for year 1052 of (a) the zonally-averaged zonal flow near the surface and in the interior (b) the vertically-averaged (top 165m) quasi-geostrophic potential vorticity gradient and (c) the interior quasi-geostrophic potential vorticity gradient. The vertical scale of (b) and (c) are different. Note that the near-surface gradient shown in (b) includes the contribution from the surface temperature gradient in the surface "PV sheet" and, in fact, is dominated by that contribution.

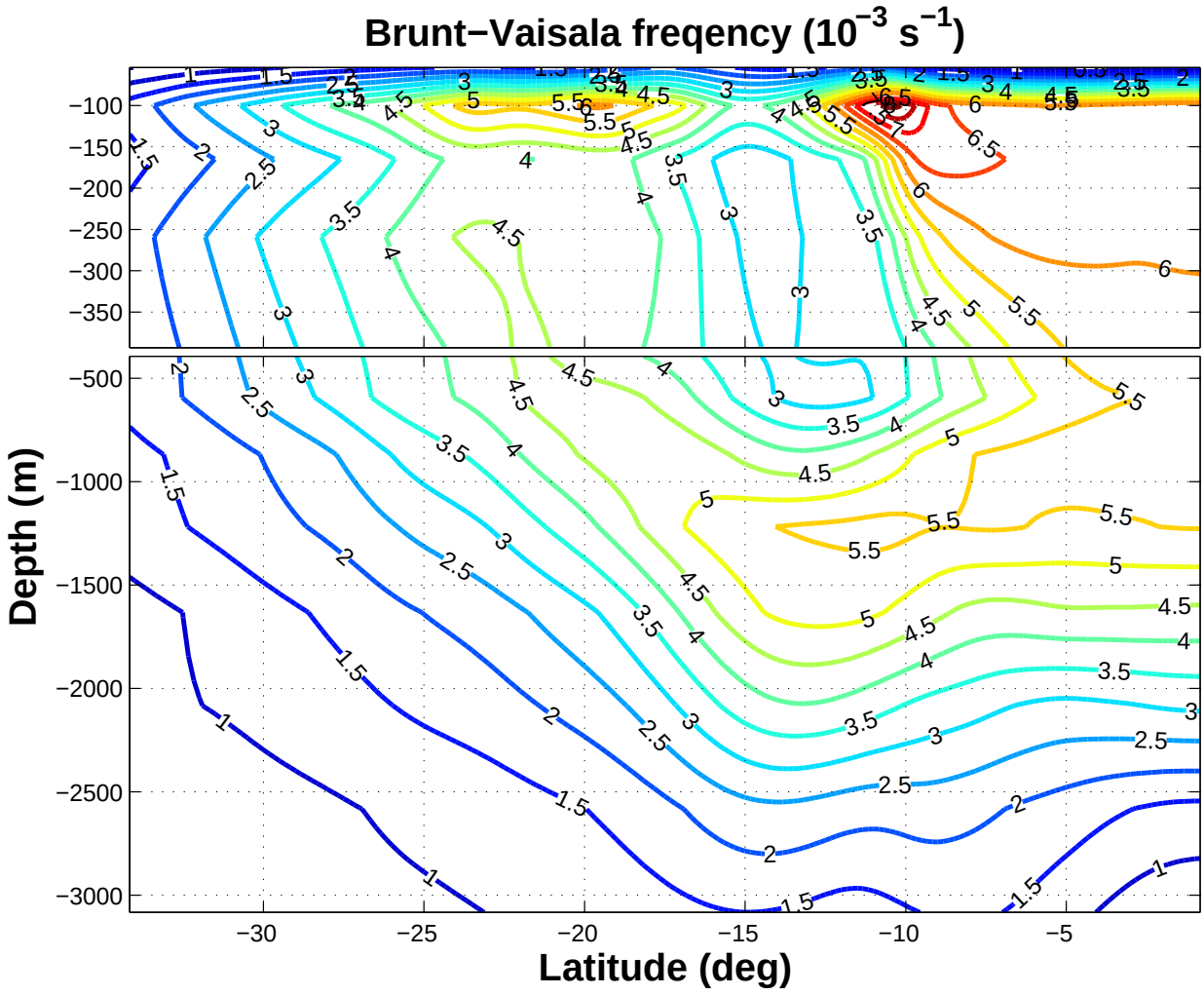

Figure 5: Time-averaged static stability ($10^{-3}s^{-1}$).

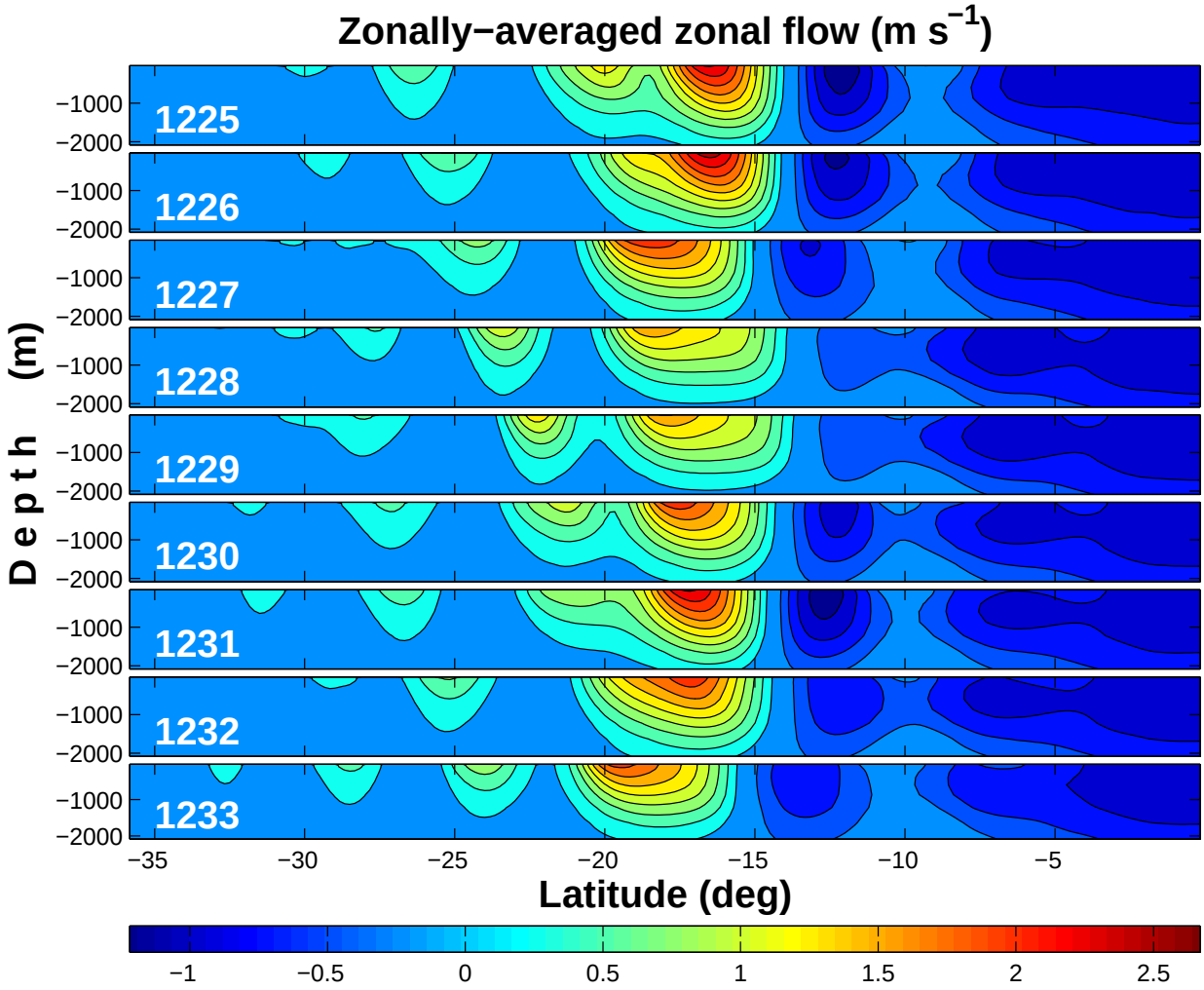

Figure 6: Time series of the annually-averaged zonally-averaged zonal flow. Time stamps (in years) are located on bottom left corner of each plot. Contour interval is 0.25 m s^{-1} and the zero contour is omitted.

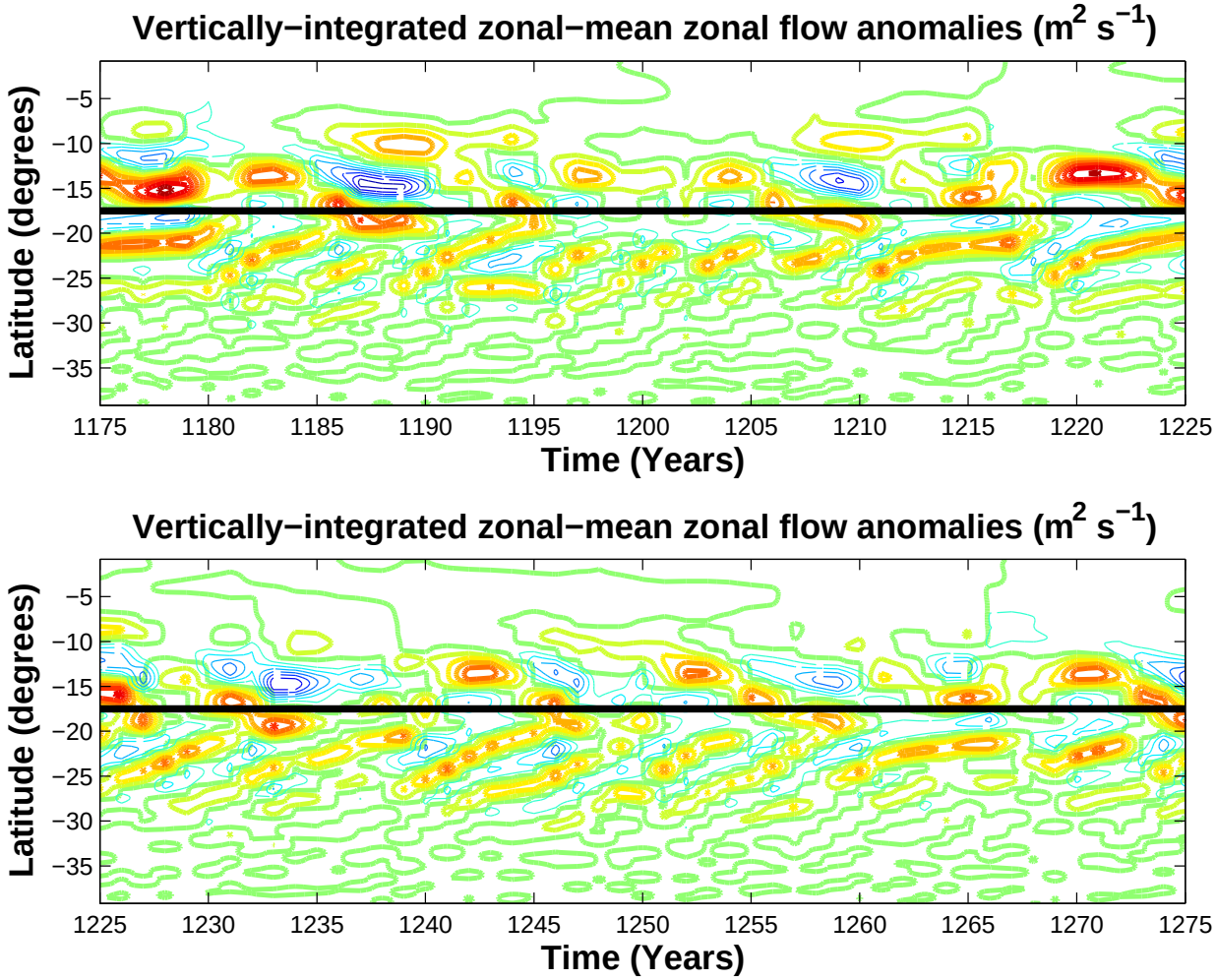

Figure 7: Time series of the anomalous vertically-integrated zonally-averaged zonal flow. Positive contours start at 20 and increase in increments of 200. Negative contours (dashed lines) start at -200 and are also in increments of 200. Thick black line represents the time-averaged position of the main jet.

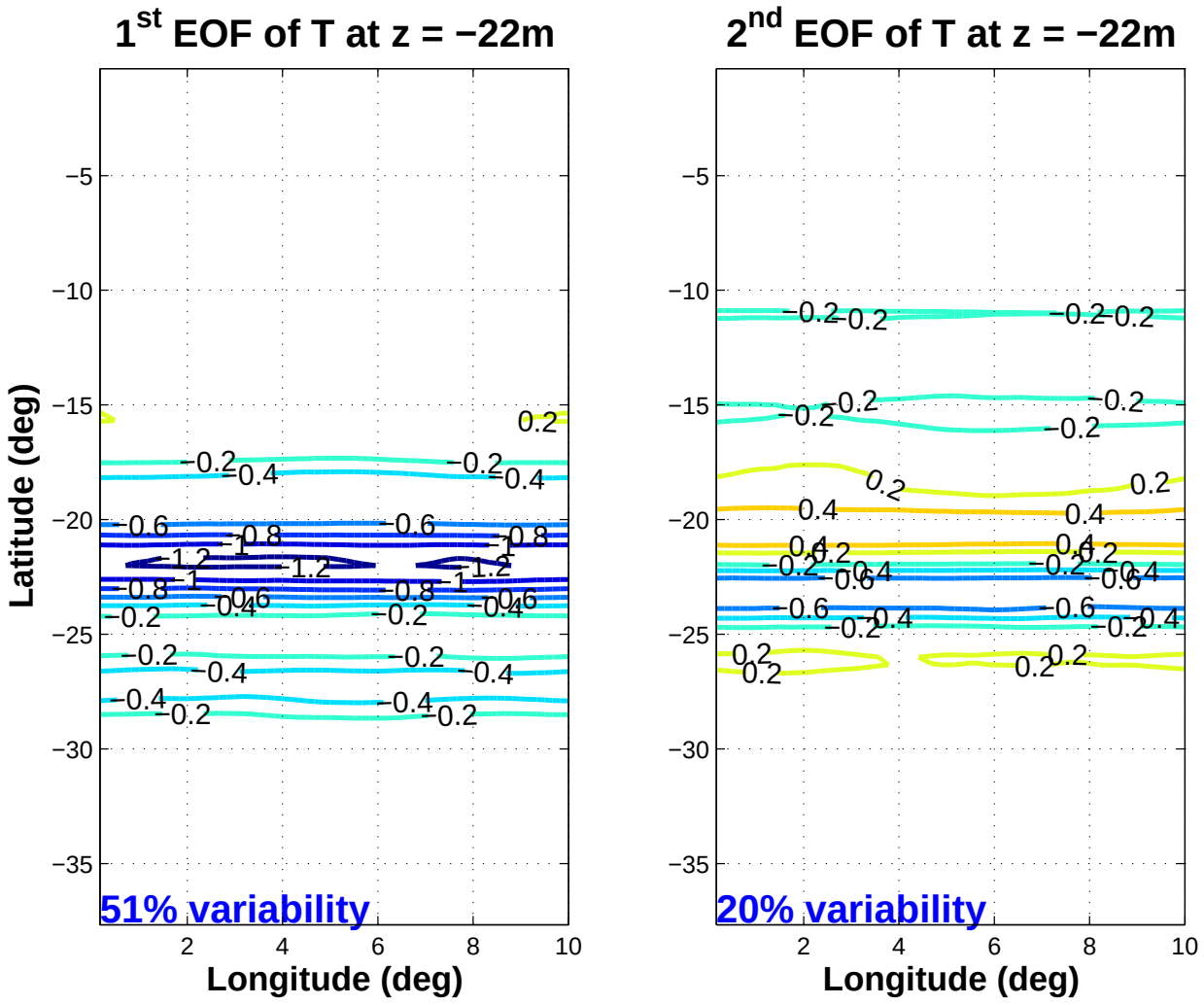

Figure 8: The leading two EOFs of the annually-averaged temperature at the surface layer. The percent variance is shown in the bottom left corner.

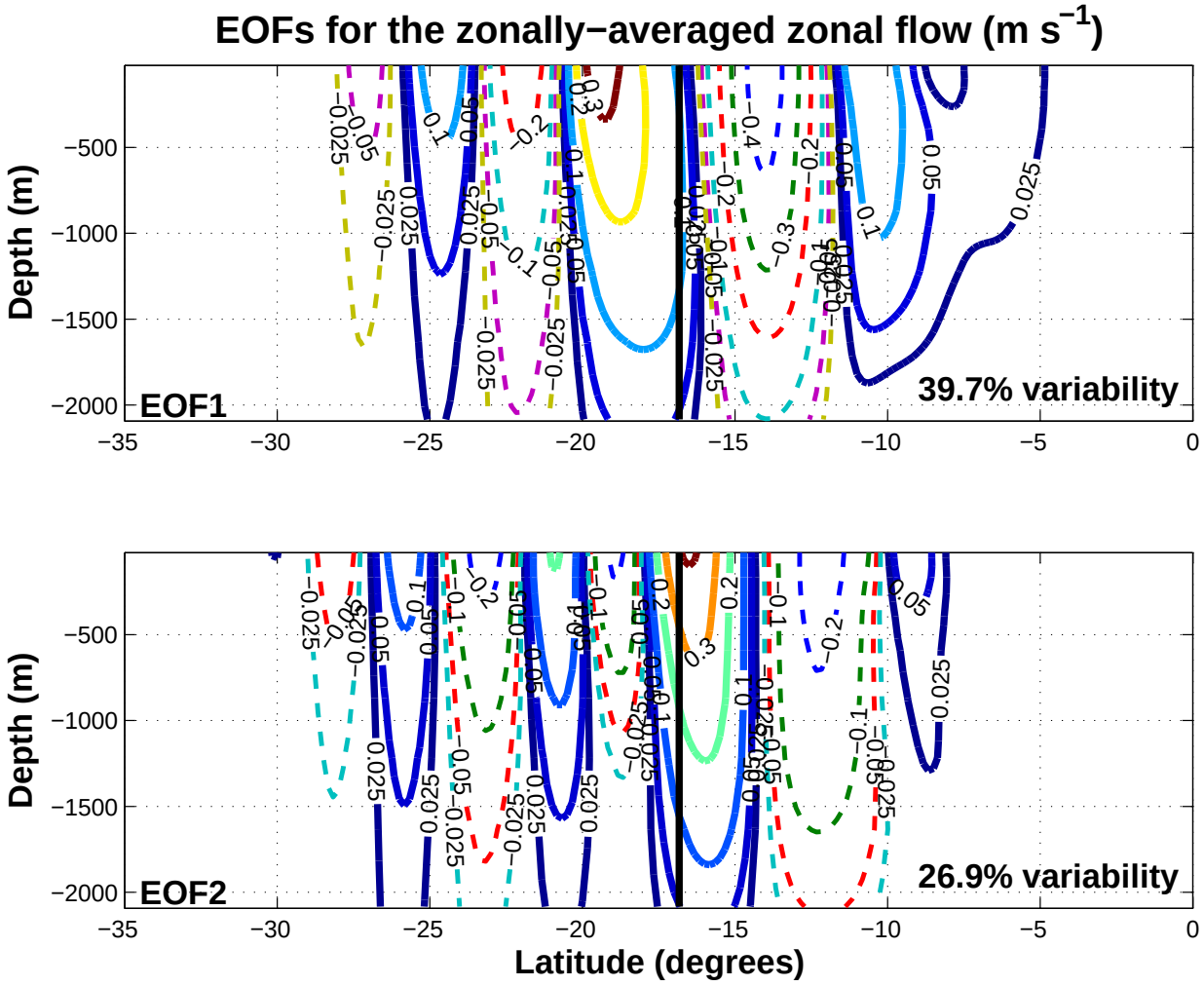

Figure 9: The leading two EOFs of the annually-averaged zonal-mean zonal flow. Solid (dashed) lines represent positive (negative) values. Note the nonuniform contour interval. Vertical black line indicates position of the time-averaged jet. The percent variance is shown in the bottom right corner.

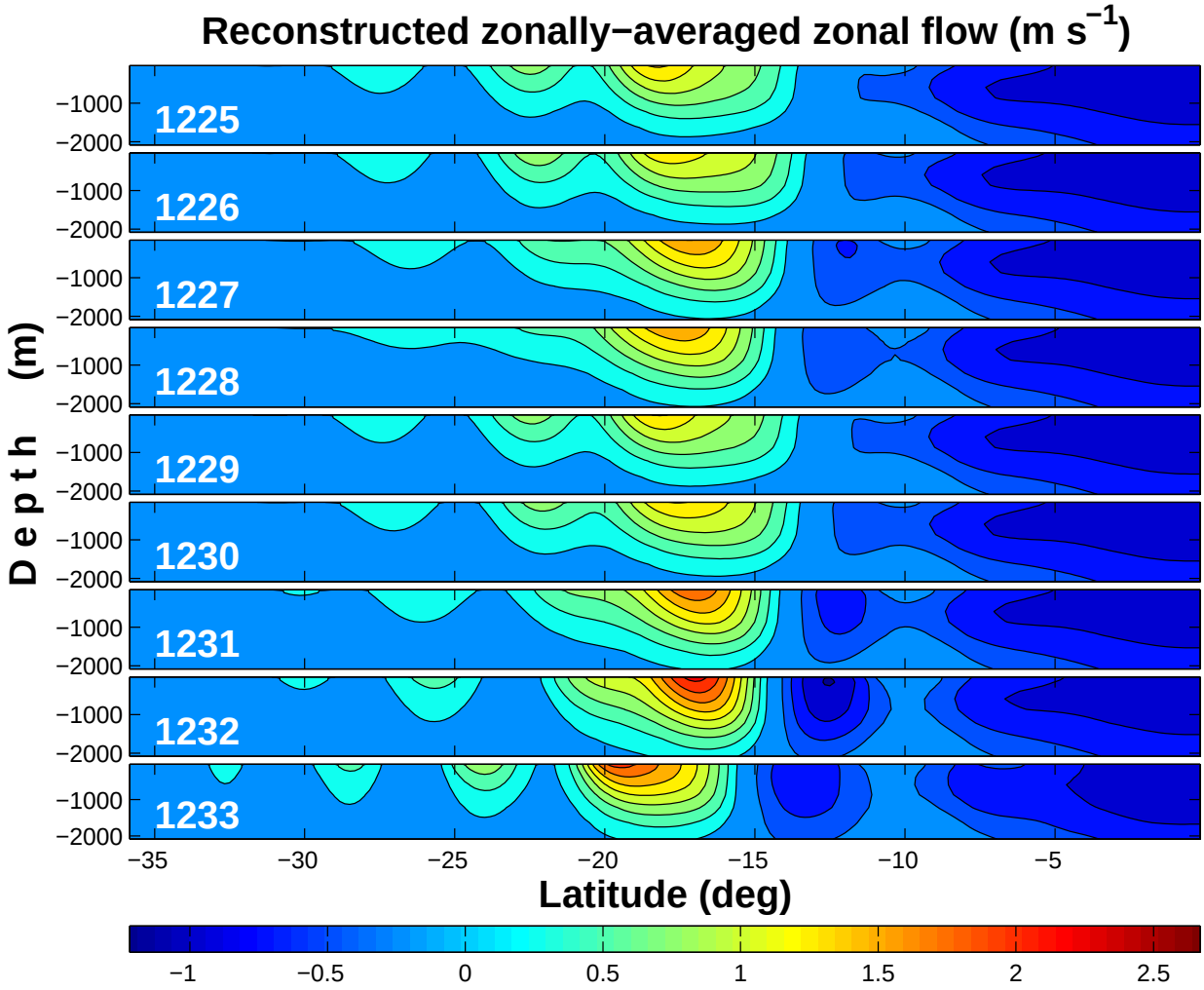

Figure 10: Time series of the reconstructed zonal flow using the leading two EOF modes and the time-averaged zonal flow.

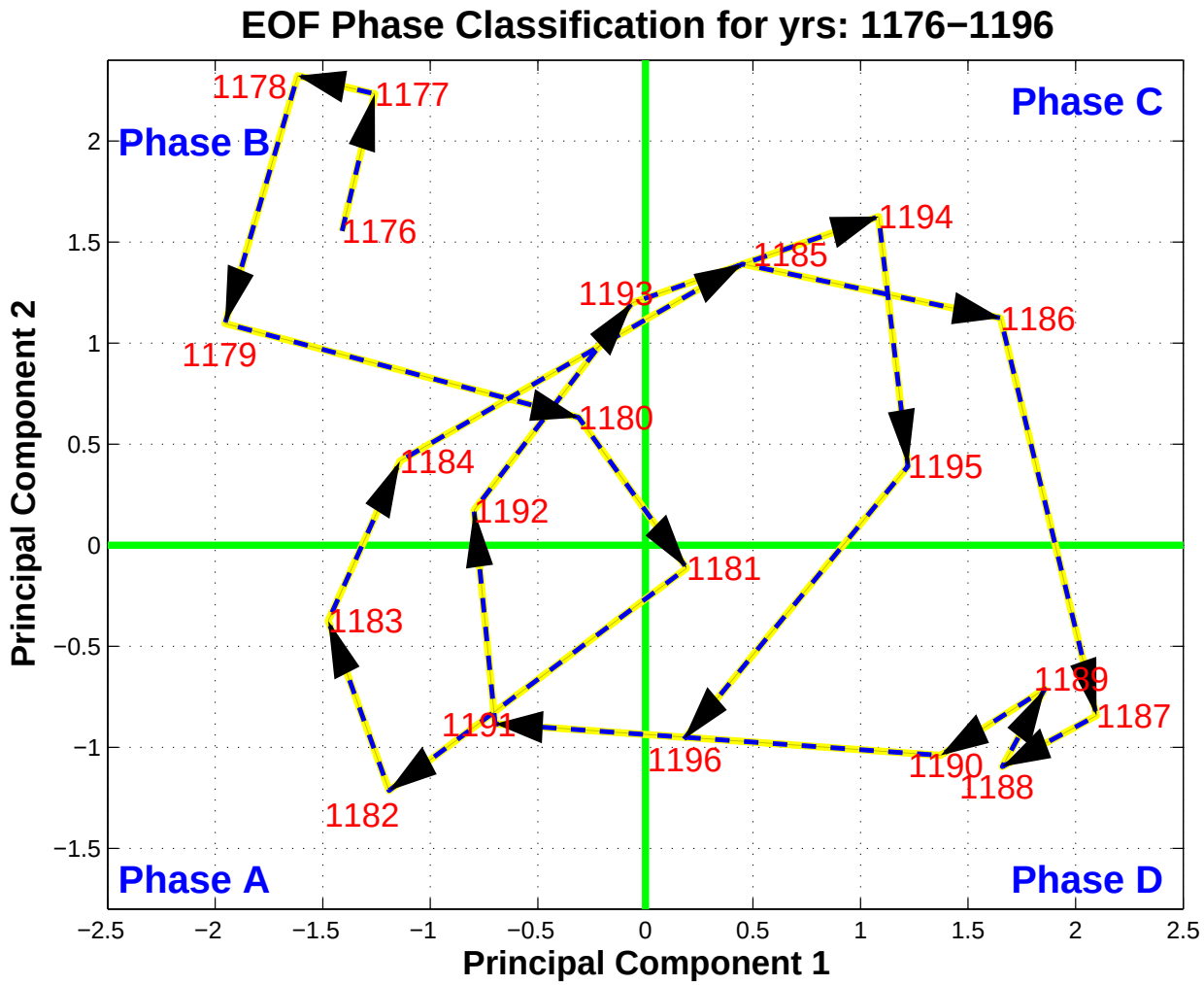

Figure 11: The time series of the leading two principal components in PC space. The EOF phases are described in Table 1 and labelled in each quadrant. Each point is a one year average.

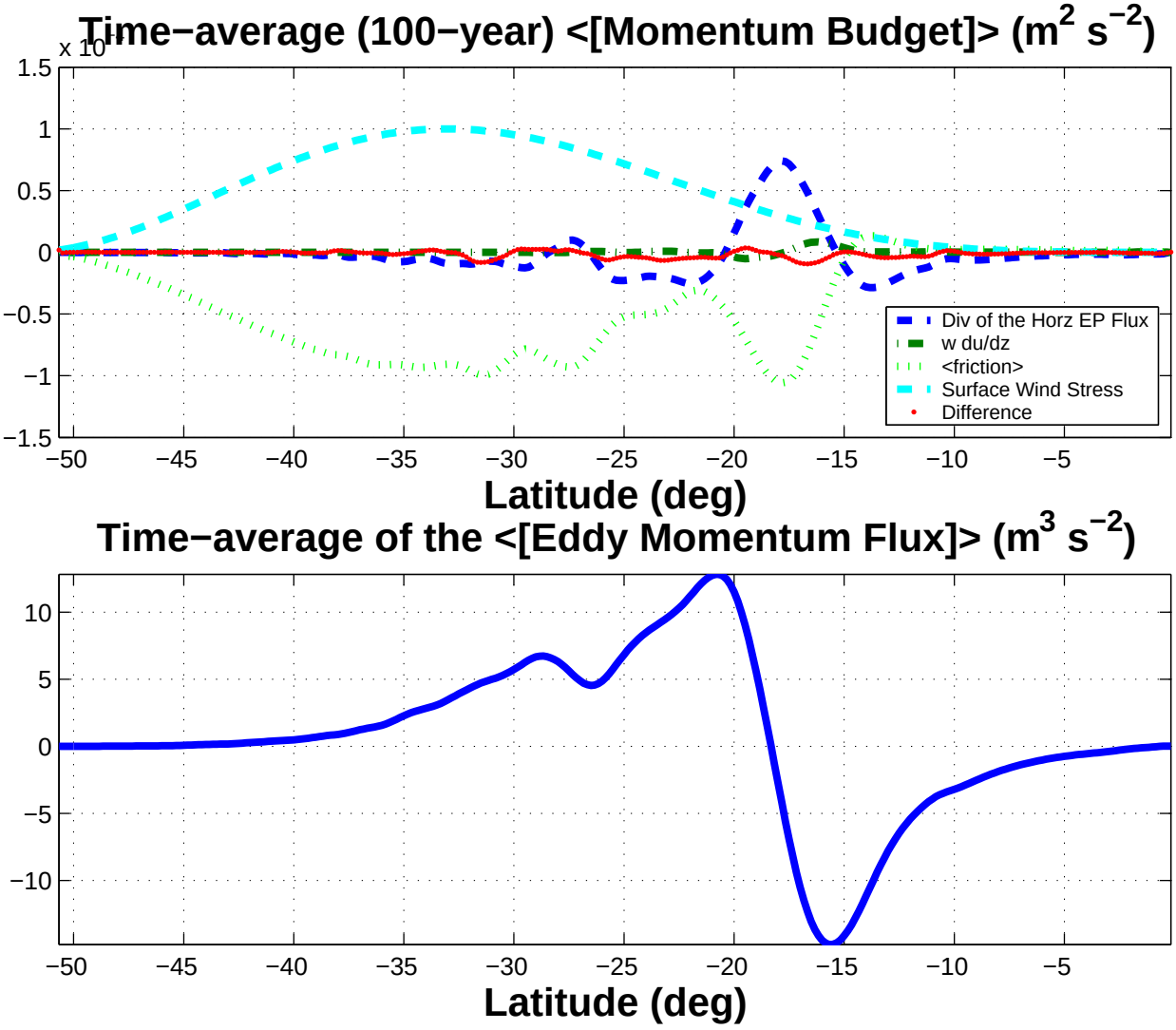

Figure 12: (a) Time-averaged quantities of the vertically-integrated zonally-averaged zonal momentum budget. Adapted from Cerovecki et al. (2007) (b) Time average of the vertically-integrated eddy momentum flux $< [u'v'] >$.

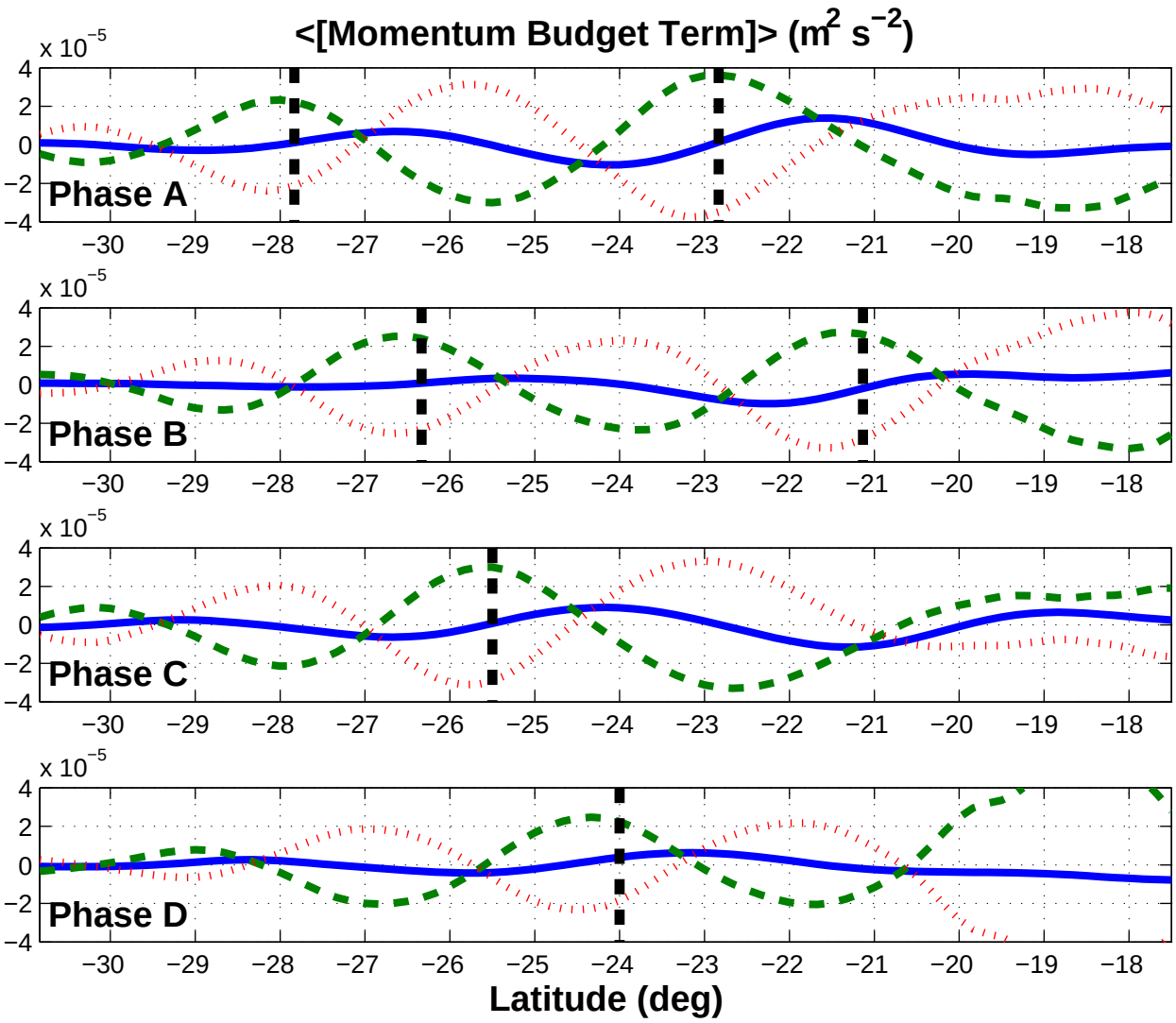

Figure 13: Anomalous quantities of the vertically-integrated zonally-averaged zonal momentum budget for each EOF phase composite labelled at the bottom left corner of each plot. Blue (solid) line is the flow tendency; green (long dashed) line is the eddy momentum flux convergence; red (vertically dashed) line is the friction. Black (vertical) dashed lines correspond to the maximum positive zonal flow anomalies.

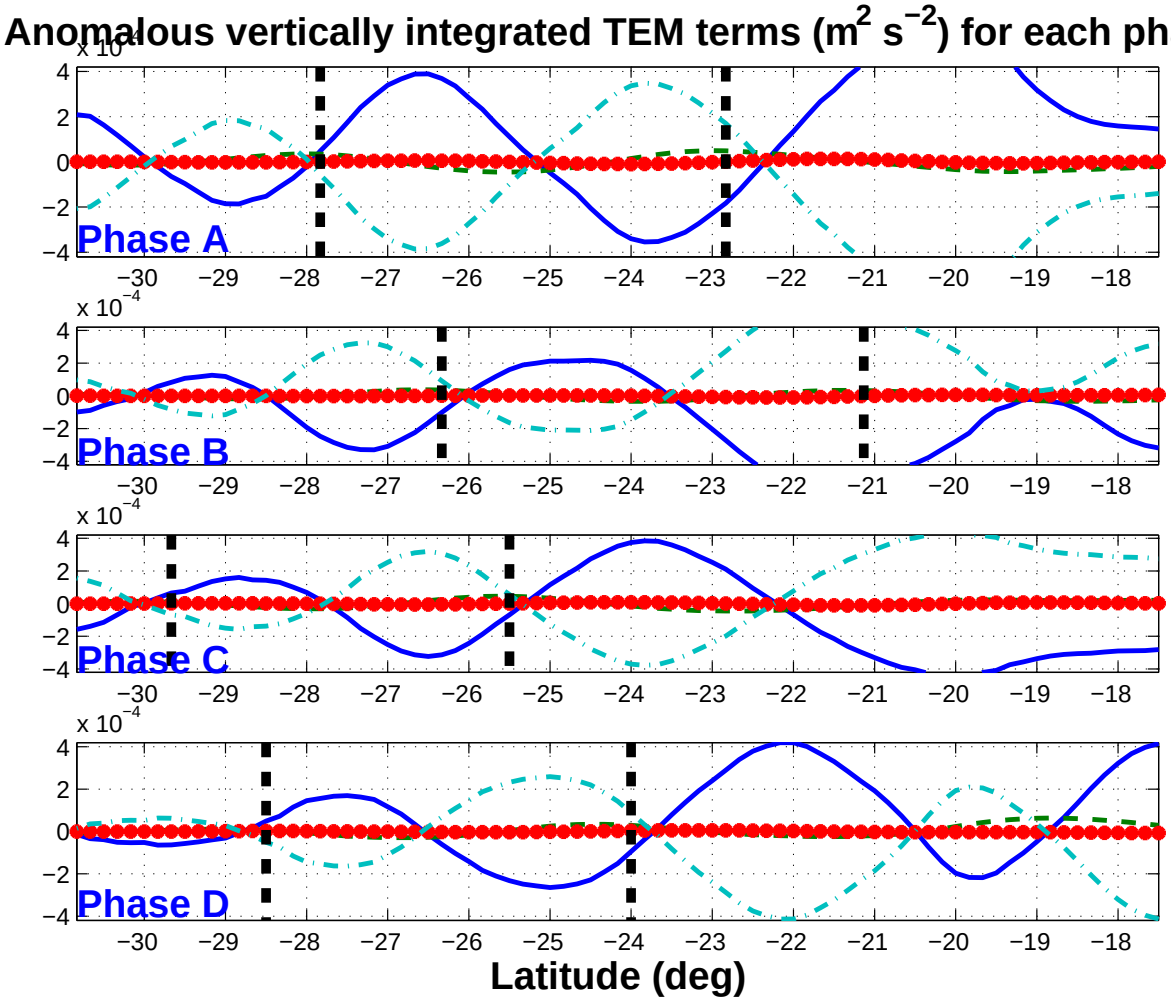

Figure 14: Anomalous quantities of the vertically-integrated TEM equation for each phase. The vertical integral was taken from the surface to a depth of 1600m. Blue (solid) line is the divergence of the vertical component of the EP flux; green (long dashed) line is the divergence of the horizontal component of the EP flux; red (dotted) line is the flow tendency; and the cyan (dot-dashed) line is the Coriolis force. Black (vertical) dashed lines correspond to the maximum positive zonal flow anomalies.

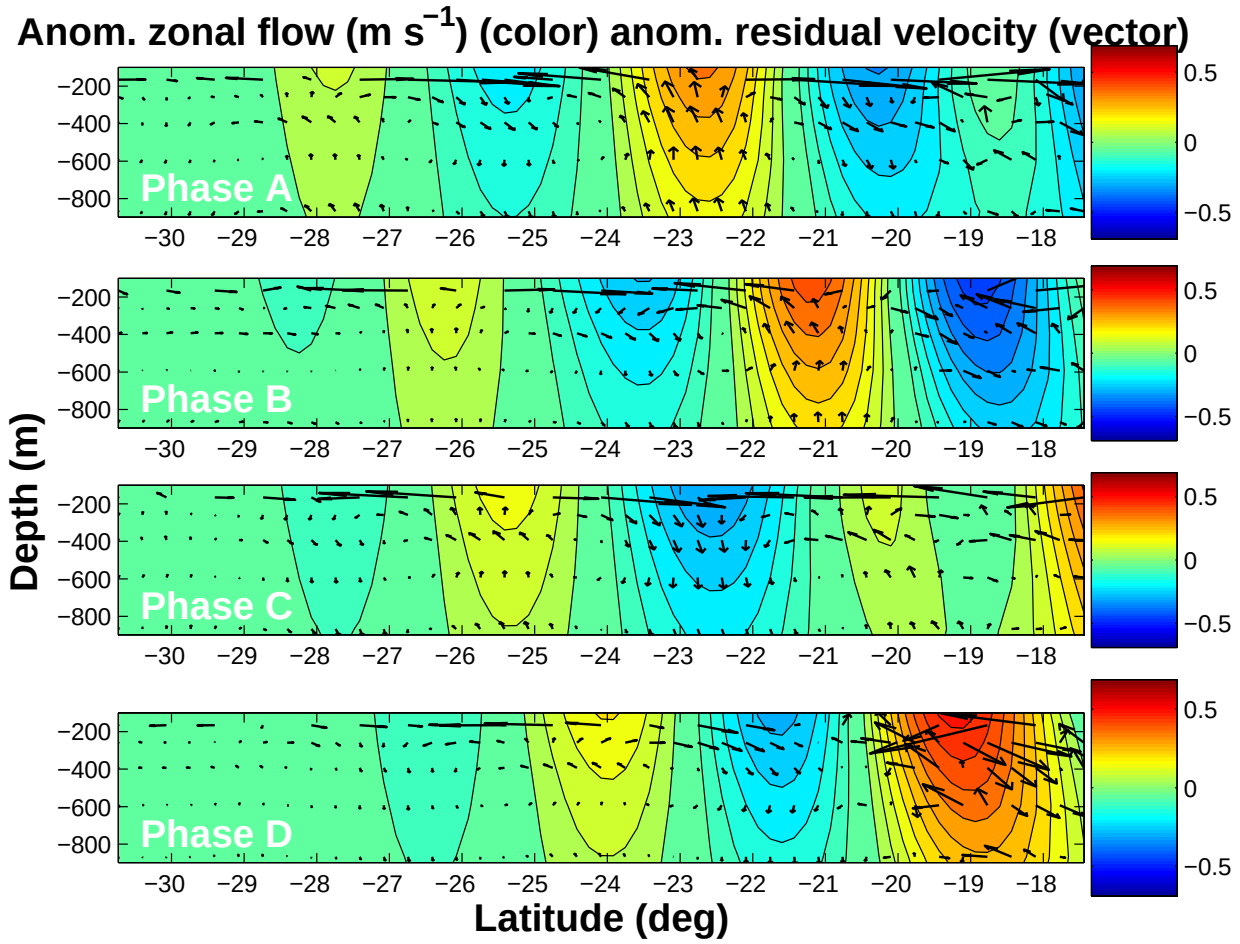

Figure 15: Anomalous residual circulation (vector) plotted over anomalous zonal flow (color) for each phase. The vectors are scaled the same for each plot, with the largest vector corresponding to 1.33 cm sec^{-1}.

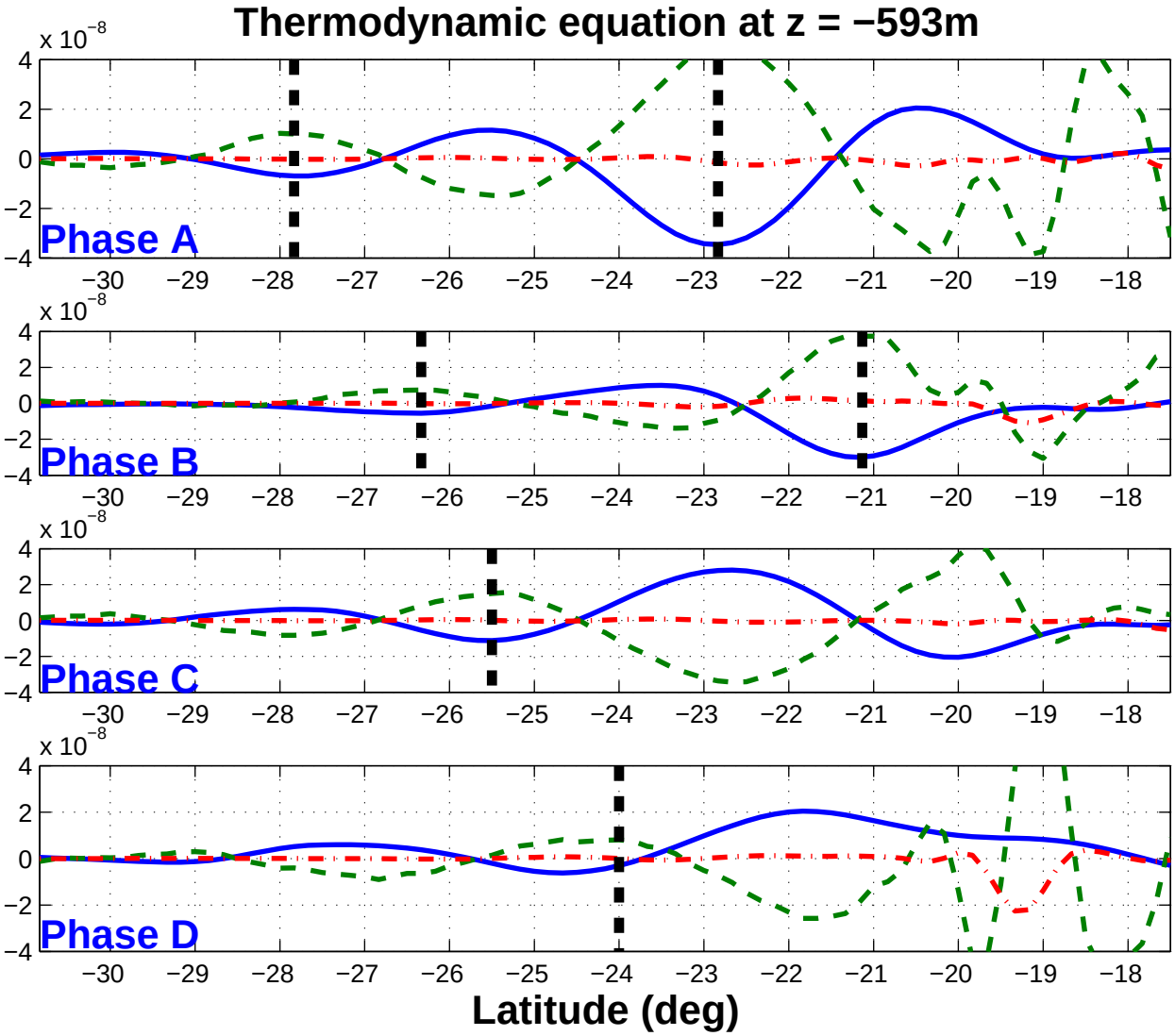

Figure 16: Anomalous quantities of the transformed Eulerian mean thermodynamic equation (^{o}C s^{-1}) at z=-593m. Blue (solid) line is the temperature tendency; green (long dashed) line is the residual vertical advection of the vertical temperature gradient; red (dot dashed) line is the residual meridional advection of the meridional temperature gradient. Black (vertical) dashed lines correspond to the maximum positive zonal flow anomalies.

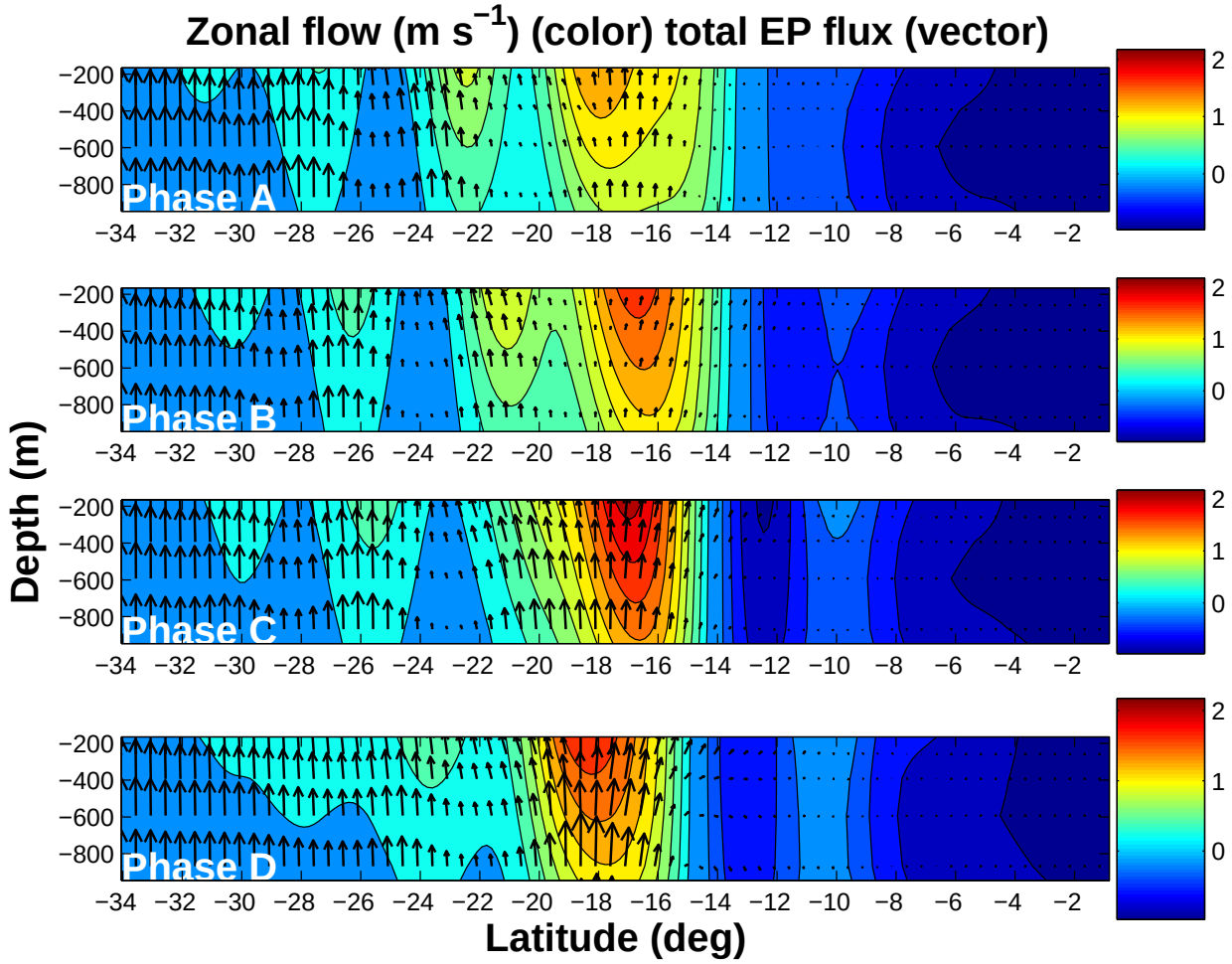

Figure 17: The total EP flux vectors for each EOF phase composite (labelled on bottom left corner) along with the zonally-averaged zonal flow. The vectors are scaled the same for each plot.

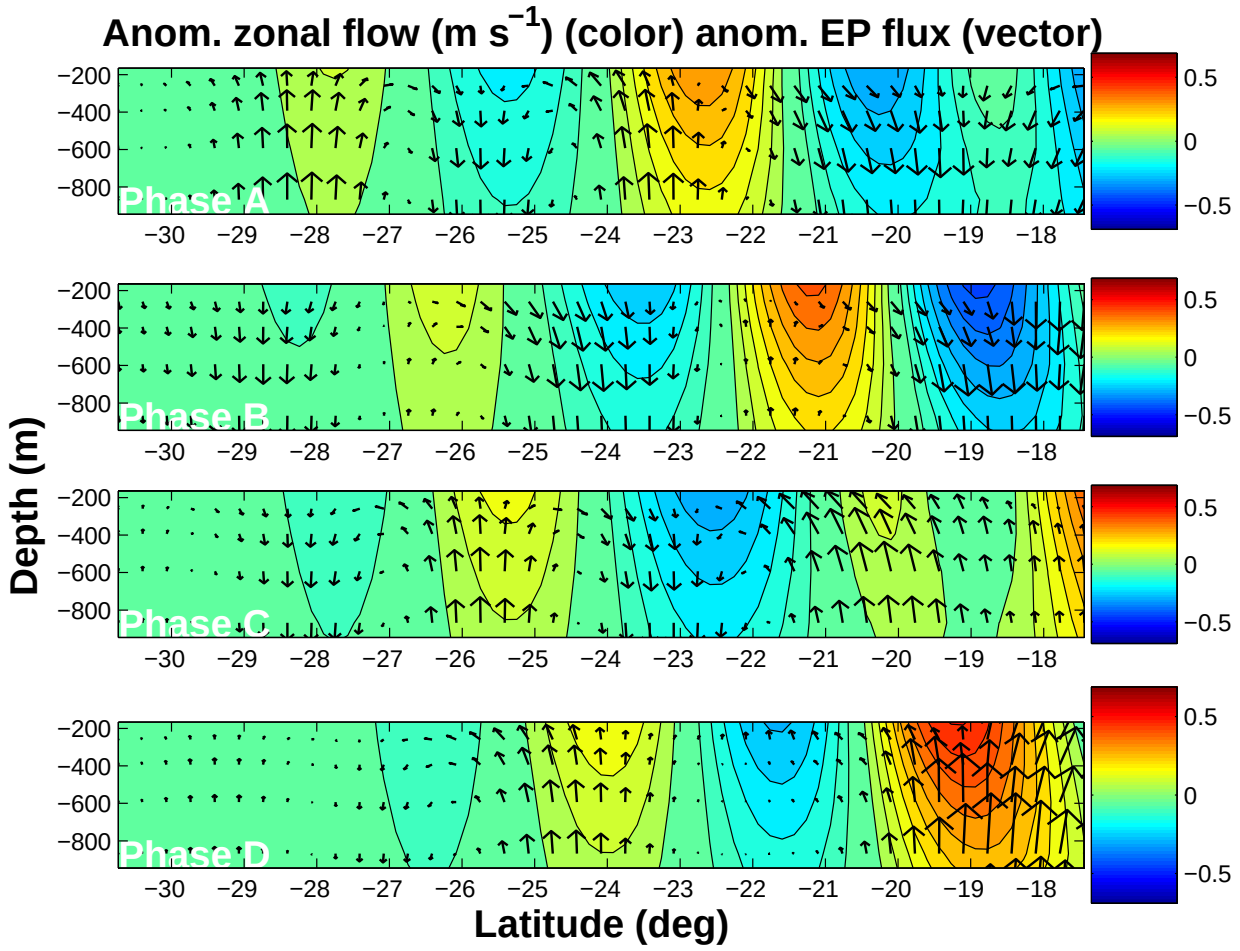

Figure 18: Anomalous EP flux vectors for each EOF phase composite are plotted over the zonally-averaged zonal flow anomalies. Each phase is labelled at the bottom left corner of plot. The vectors are scaled twice as large as Fig. 17 and are the same for each plot.

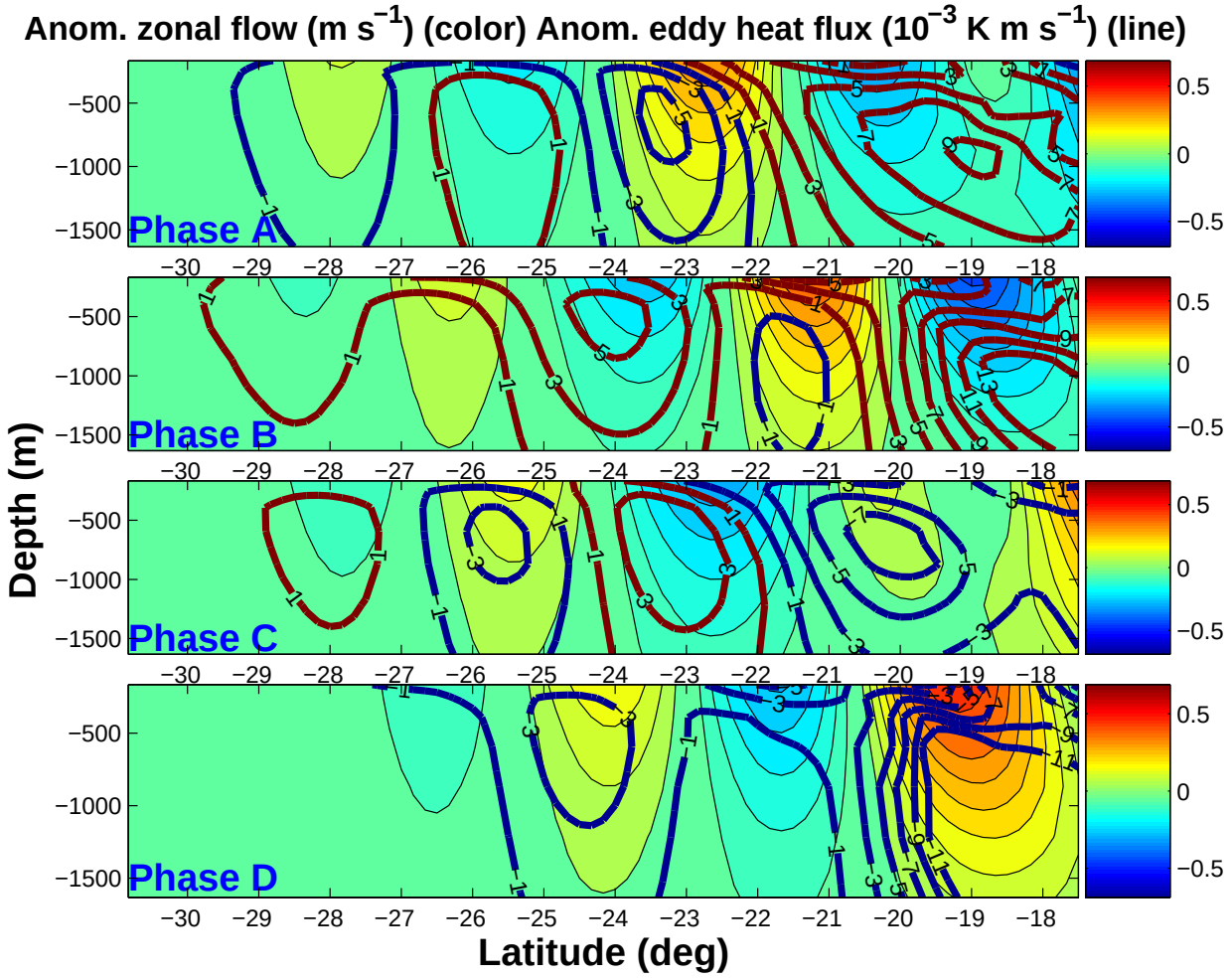

Figure 19: Anomalous eddy heat flux (line) is plotted over zonal flow anomalies (in color). Each phase is labelled at the bottom left corner of plot.

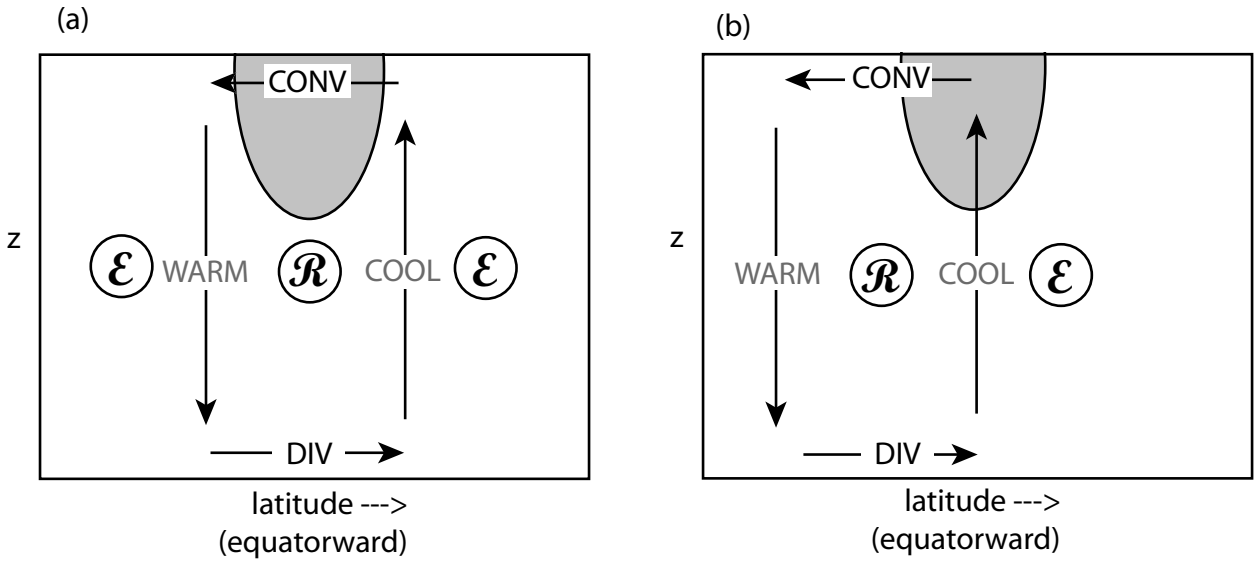

Figure 20: Schematic depiction of the interaction between baroclinic eddies and a localized jet. In frame (a), the baroclinic eddy activity is assumed to be symmetric about the jet; in (b), it is stronger on the poleward flanks of the jet, presumed to be a consequence of a general poleward decrease of static stability. 'CONV' and 'DIV' denote convergence and divergence, respectively, of the baroclinic EP fluxes; 'COOL' and 'WARM' indicate the local temperature tendencies attributable to the induced residual circulation, thus reducing ($\mathcal{R}$) and enhancing ($\mathcal{E}$) the local zonal mean baroclinicity. (Note that the southern hemisphere is depicted; the equator is to the right.) See text for discussion.

Table 1: Physical characteristics of the primary jet in the four EOF phases.

	Phase A	Phase B	Phase C	Phase D
PC1	Negative	Negative	Positive	Positive
PC2	Negative	Positive	Positive	Negative
Displacement	Equatorward	Equatorward	Poleward	Poleward
Strength	Decreasing	Increasing	Increasing	Decreasing

Table 2: Statistical results on the conditions prior to the onset of each phase and zonal index.

	Phase A	Phase B	Phase C	Phase D
Prior to Phase A	–	7%	29%	64%
Prior to Phase B	85%	–	15%	0%
Prior to Phase C	16%	79%	–	5%
Prior to Phase D	19%	6%	75%	–
Prior to High Zonal Index	26%	74%	–	–
Prior to Low Zonal Index	–	–	39%	61%